cite as: Hagen, Christopher L., "Fundamentals of Transient Thermal-Light Absorption Spectroscopy and Application to Optical Sensing in HCCI Engines," Ph.D. Thesis, University of Wisconsin-Madison, 2006 (http://digital.library.wisc.edu/1793/35127)

FUNDAMENTALS OF TRANSIENT THERMAL-LIGHT ABSORPTION SPECTROSCOPY AND APPLICATION TO OPTICAL SENSING IN HCCI ENGINES

by

Christopher L. Hagen

A dissertation submitted in partial fulfillment of

the requirements for the degree of

Doctor of Philosophy

(Mechanical Engineering)

at the

UNIVERSITY OF WISCONSIN-MADISON

2006

FUNDAMENTALS OF TRANSIENT THERMAL-LIGHT ABSORPTION SPECTROSCOPY AND APPLICATION TO OPTICAL SENSING IN HCCI ENGINES

Christopher L. Hagen

Under the supervision of Assistant Professor Scott T. Sanders

At the University of Wisconsin – Madison

Abstract

A set of equations is developed for evaluating absorption spectroscopy based on thermal emitters such as lamps. The noise sources considered are photon (shot) noise and beating (wave interference) noise; signal-to-noise ratio limits for transient sensing with thermal light are also defined as a result of the analysis herein.

The set of equations developed is used to evaluate three real absorption experiments: one which uses a thermal emitter, another which uses an external cavity diode laser, and one more which uses a supercontinuum source. In each experiment species concentration measurements are made in a homogenous charge compression ignition engine.

Table of Contents

List of Figures

List of Tables

Nomenclature

$\#_{res\ elements}$	Number of resolution elements covered in a spectrum [-] Example: a spectrum from 1000 – 1100 [nm] measured with 1 [nm] spectral resolution has $\#_{res\ elements}$ = 100.
A	Area [m^2].
A_d	Photodetector area [m^2].
c	Speed of light in a vacuum 3E+8 [$m\ s^{-1}$].
color temperature	The black body temperature where the maximum emission wavelength is the same as a real thermal emitter.
C	Capacitance [F].
CAD	Engine crank angle degree.
chirped light	A scan of light either increasing or decreasing in optical frequency with respect to time (i.e., temporal spectral dispersion).
D^*_{BLIP}	Normalized detectivity for a background limited infrared photodetector [$cm\ Hz^{1/2}\ W^{-1}$].
FWHM	Full width at half maximum.
h	Planck's constant 6.626E-34 [$m^2\ kg\ s^{-1}$].
H_2O	Chemical formula for water.
H_2O_2	Chemical formula for hydrogen peroxide.
HCCI	Homogeneous charge compression ignition.
I	Recorded transmitted light intensity [V].

I_o	Recorded incident light intensity [V].
k	Boltzmann constant 1.38E-23 [m^2 kg s^{-2} K^{-1}].
k_1	Constant 1.05E+17 [$m^{-3}s^{-1}K^{-4}$].
k_2	Constant 4716 [$m^{-2}K^{-2}$].
k_3	Constant 22 [m^2Hz].
k_4	Constant 103750 [HzK^{-2}].
k_5	Constant $1/2\pi$ [-].
k_6	Constant 2.218 [-].
k_7	Constant 7.624E+10 [Hz].
k_{Wien}	Wien's displacement law constant 0.003669 [m-K].
MDA	Minimum detectable absorbance [-] (analogous to SNR for spectroscopy).
$MDA_{broadened}$	Instrument broadened minimum detectable absorbance [-].
MDA_{FR}	Fully resolved minimum detectable absorbance [-].
$M_{p,\lambda}$	Spectral photon flux density [photons m^{-2} m^{-1} s^{-1}] (where m^{-2} refers to emitter area and m^{-1} refers to wavelength).
n_p	Number of photons [photons].
$\overline{n_p}$	Mean number of photons incident on the detector during the sample time [photons].
R	Resistance [Ω].
SNR	Signal-to-noise ratio [-].
SNR_{beat}	Beating (interference) signal-to-noise ratio [-].

$SNR_{broadened}$	Instrument broadened signal-to-noise ratio [-].
SNR_{FR}	Fully resolved signal-to-noise ratio [-].
SNR_{max}	Maximum signal-to-noise ratio [-].
SNR_{photon}	Signal-to-noise ratio due to photon noise [-].
$SNR_{photon\ max}$	Maximum signal-to-noise ratio due to photon noise possible for a black body at T_{BB} [-].
T_{BB}	Temperature of black body [K].
$\overline{trans}$	Mean transmission [-].
$\Delta\nu_{feature}$	Spectral width of absorption feature of interest [Hz].
$\Delta\nu_{res}$	Spectral resolution of an instrument [Hz].
$\Delta\nu_{total}$	Complete spectral range covered by a measured absorption spectra [Hz]. Example: the measurement of a spectrum spanning 3E+14 - 2.7E+14 [Hz] (1000-1100 [nm]) has a $\Delta\nu_{total}$ = 3E+13 [Hz].
ΔE	Uncertainty in energy [J].
Δf	Bandwidth for measuring a single spectral element [Hz]. Example: a spectrum from 1000 – 1100 [nm] measured at 1000 [Hz/spectrum] with 1 [nm] spectral resolution ($\Delta\nu_{res}$) will have Δf = 100000 [Hz].
Δf_{total}	Acquisition frequency for complete spectra [Hz]. Example: Δf_{total} = 1000 [Hz] for the example in Δf above.
Δt	Time to sample a single spectral element [s].
$\Delta\lambda_{res}$	Spectral resolution of a single spectral element [m].

η	Quantum efficiency [%].
$\theta_{1/2}$	Viewing half angle [degrees].
λ	Wavelength [m], $\lambda = c/\nu$.
λ_{max}	Wavelength of maximum photon flux density [m].
ν	Optical frequency [Hz], $\nu = c/\lambda$.
ν	Vibrational band assignment. Example: $\nu_1 + \nu_3$ is a combination band in H_2O vapor commonly used for sensing.
π	Constant 3.1416 [-].
σ_p	Uncertainty in the arrival of photons [photons].
σ_{trans}	Transmission uncertainty [-].
φ_p	Photon flux [photons/s].

Chapter 1 Introduction

The work by the author prior to the composition of this thesis consisted of multiple broad-wavelength highly-transient absorption measurements in homogenous charge compression ignition (HCCI) engines based upon the foundation laid by Sanders[1] and Kranendonk[2]. For example, in Appendix III spectra spanning 1380 – 1850 [nm] were measured every 5 [μs] with a 0.1 [nm] spectral resolution. During this work the performance fundamentals of such measurements were not well understood. Work progressed under the assumption that rapid coverage of broad spectra with high spectral resolution was desirable and detection sensitivity was initially given minor consideration. However, the importance of detection sensitivity, or minimum detectable absorbance (*MDA*), was revealed by the experiments. The purpose of this thesis is to illustrate the fundamental limits of *MDA* bounded by the noise properties of a thermal emitter. A thermal emitter is a light source whose radiative properties are governed by Planck's distribution[3].

Though the topics covered in this thesis are diverse, the subject matter is largely covered by the study of optical radiation detection and spectroscopy. For a thorough treatment of optical radiation detection the reader is encouraged to see[4, 5]. Regarding spectroscopy, the author has used many references, but recommends Atkins[6] as a general source.

Section 1.1 Motivation

This thesis contains detailed treatment of material which may be unfamiliar to the reader; however, the key points to be understood are the following:

- Beating noise, rather than photon noise, generally dominates in high-speed spectroscopy experiments.
- Laser sources outperform thermal emitters because of higher coherence and irradiance.
- Spectral resolving potential is decreased as minimum detectable absorbance (*MDA*) is decreased. Increases in either the spectral range or the rate at which spectra are collected will also decrease spectral resolving potential.
- Light dispersed by a diffraction grating onto an array of detectors outperforms temporally dispersed (chirped) light recorded by a single detector.
- Thermal light detected in the limit of the Heisenberg uncertainty principle will have a signal-to-noise ratio (*SNR*) < 1.49.

The list above is not comprehensive, but highlights the author's findings.

Section 1.2 Thesis Overview

The progress of this thesis is as follows. The noise sources to be considered are introduced in Chapter 2. Next, in Chapter 3 a set of additional relationships are introduced so that Chapter 2 material can be applied to spectroscopy. Then, real

specifications are used in sample calculations in Chapter 4. The Heisenberg uncertainty principle is considered in Chapter 5 and closing thoughts are discussed in Chapter 6. After the chapters, the three related experiments referred to throughout the thesis are included as appendices.

Chapter 2 Optical Noise

Section 2.1 Introduction

In this chapter two thermal emission noise sources, photon noise and beating noise, are discussed along with their relationship to signal-to-noise ratio (*SNR*). In the case of photon noise, a simplified equation is developed. The equation for beating noise is introduced directly from the reference. Next, the two noise equations are combined and compared with experiments from the author. The chapter is concluded with a discussion of each experiment's performance relative to its predicted thermal emitter performance.

Section 2.2 Photon (Shot) Noise

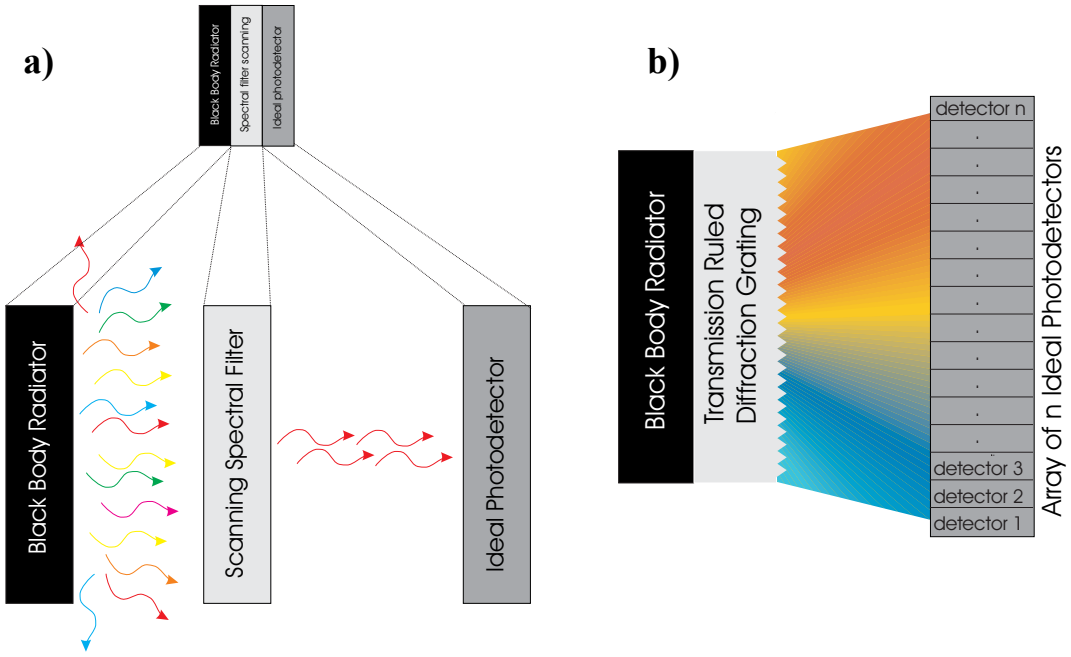

Figure 2.2.1a) <u>Temporal Spectral Dispersion (Chirped Light)</u>: Schematic of a black body radiator which is scanned by a spectral filter and recorded by an ideal detector. The black body has a temperature T_{BB}, the spectral filter has a spectral pass band of $\Delta\lambda_{res}$ which it scans in Δt, and the detector has an area of A_d. b) <u>Spatial Spectral Dispersion</u>: Schematic (simplified) of a black body radiator dispersed by a grating unto an array of n ideal photodetectors (pixels). The black body temperature is T_{BB}, the spectral resolution of the grating/array is $\Delta\lambda_{res}$ which is integrated over Δt, and each detector has an area A_d.

Photon noise (or shot noise) is discussed here from the limiting situation of all photons from a black body radiator being scanned in time or space (Figure 2.2.1a and b) and

captured by an ideal photodetector. An ideal photodetector, as used here, has the attributes listed in Table 2.2.1.

Table 2.2.1 Attributes of ideal detector used for photon noise equation development

Viewing half angle, $\theta_{1/2}$	Signal to noise ratio, *SNR*	Quantum efficiency, η	Bandwidth, Δf
[degrees]	[1]	[%]	[Hz]
90	∞	100	∞

For a discussion of photon noise in a real detection system see[5].

Photon noise is the noise generated due to the discrete nature of light. That is, if light is measured on a very short time scale, the impact of each individual photon can be detected. An effective analogy for photon noise is the sound of rain drops on a metal roof. If the rain drops are sparse, it is easy to distinguish the striking of an individual drop. However, as the number of drops striking the roof over a fixed amount of time increases (i.e., drops/s), the sound of the individual is blended with the others.

Bench top experiments can be executed over several minutes with large detectors. In this case, the number of photons collected is sufficient so that photon noise is not a limiting factor. However, fast measurement systems do not have the benefit of either time (~GHz bandwidth) or area (A_d generally << 1 mm^2) for collecting photons. Here a relationship will be derived to quantify the contributions of measurement bandwidth and detector area

to photon noise when measuring a thermal emitter. It will also be shown that spectral resolution is a contributor.

This discussion of photon noise begins by stating that the probability of n_p photons being emitted in a time period Δt can be estimated using a Poisson distribution[7]. Dereniak and Crowe[5] show that, because of the Poisson distribution and by neglecting the Boson factor, the following relationships apply.

$$SNR_{photon} = \sigma_p = \sqrt{\overline{n_p}} = \sqrt{\phi_p \Delta t} \qquad \textbf{(2.2.1)}$$

Where SNR_{photon} [-] is the signal to noise ratio due to photon noise, σ_p [photons] is the square root of the variance of the Poisson distribution describing the arrival of photons, $\overline{n_p}$ [photons] is the average number of photons incident on the detector in time period Δt, φ_p [photons s^{-1}] is photon flux, and Δt [s] is the time period of interest.

Next, more insight into (2.2.1) is given by expanding the photon flux.

$$\phi_p = \int_{\lambda_1}^{\lambda_2} M_{p,\lambda}(\lambda, T_{BB}) d\lambda A_d \qquad \textbf{(2.2.2)}$$

Where λ_1 [m] is the start of the wavelength region of interest, λ_2 [m] is the end of the wavelength region of interest, $M_{p,\lambda}$ [photons m^{-3} s^{-1}] is the spectral photon flux density, T_{BB} [K] is the temperature of the black body, and A_d [m^2] is the photodetector area.

The observation time, Δt, from (2.2.1) is cast in terms of bandwidth below for an idealized rectangular filter in the Fourier domain as detailed by Grimbleby[8] .

$$\Delta t = \frac{1}{2\Delta f} \quad \textbf{(2.2.3)}$$

Where Δf [Hz] is the detection bandwidth.

Substituting (2.2.2) and (2.2.3) into (2.2.1) we get the following.

$$SNR_{photon} = \sqrt{\frac{\int_{\lambda_1}^{\lambda_2} M_{p,\lambda}(\lambda, T_{BB}) d\lambda A_d}{2\Delta f}} \quad \textbf{(2.2.4)}$$

More specifically, $M_{p,\lambda}$ can be described by the Planck's distribution [3].

$$M_{p,\lambda}(\lambda, T_{BB}) = \frac{2\pi c}{\lambda^4 (e^{\frac{hc}{\lambda k T_{BB}}} - 1)} \quad \textbf{(2.2.5)}$$

Where c [m s^{-1}] is the speed of light in a vacuum, h [m^2 kg s^{-1}] is Planck's constant, and k [m^2 kg s^{-2} K^{-1}] is the Boltzmann constant.

The spectral photon flux density, $M_{p,\lambda}$, is seen for multiple temperatures in Figure 2.2.2.

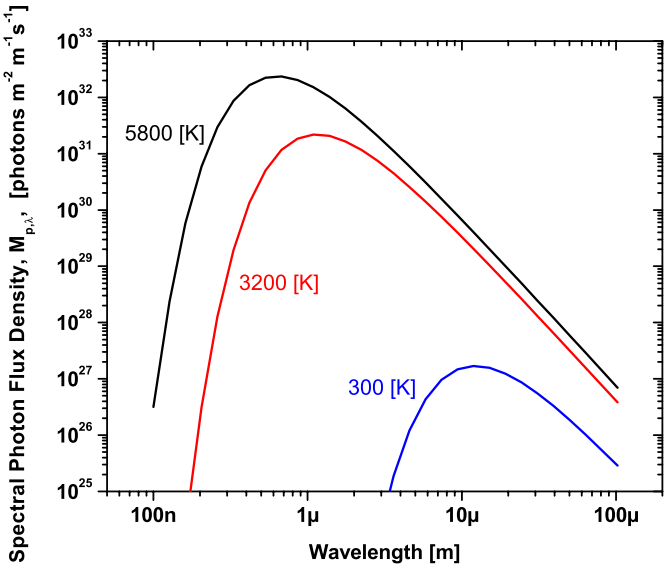

Figure 2.2.2 Planck's black body photon distribution for multiple temperatures. Note that 5800 [K] is ~ the temperature of the sun, 3200 [K] is ~ the temperature of a tungsten halogen lamp, and 300 [K] is ~ standard room temperature.

The following relationship can be deduced from (2.2.4).

$$SNR_{photon} \propto \sqrt{\int_{\lambda_1}^{\lambda_2} M_{p,\lambda}(\lambda, T_{BB})\, d\lambda} \qquad \textbf{(2.2.6)}$$

Therefore, for fixed integration limits it can be understood that the maximum SNR_{photon} occurs at the wavelength of the maximum $M_{p,\lambda}$.

$$SNR_{photon\,\max} = SNR_{photon}(\lambda_{\max}) \qquad \textbf{(2.2.7)}$$

Where λ_{max} is the wavelength of maximum $M_{p,\lambda}$ and $SNR_{photon\ max}$ is the maximum SNR_{photon} possible for thermal emitter at temperature T_{BB}.

At this point it is convenient to introduce the following approximation for determining $SNR_{photon\ max}$.

$$\int_{\lambda_{\max}-\frac{\Delta\lambda_{res}}{2}}^{\lambda_{\max}+\frac{\Delta\lambda_{res}}{2}} M_{p,\lambda}(\lambda, T_{BB})d\lambda \approx M_{p,\lambda}(\lambda_{\max}, T_{BB})\Delta\lambda_{res} \qquad \textbf{(2.2.8)}$$

Where $\Delta\lambda_{res}$ [m] is the spectral resolution for a single element of the overall measurement system.

Furthermore, the location of λ_{max}, at a given black body temperature, can be determined mathematically by differentiating (2.2.5) with respect to λ and setting the differential equal to zero. The resulting relationship is known as Wien's displacement law[9] and is shown below.

$$\lambda_{\max} T_{BB} = k_{Wien} \qquad \textbf{(2.2.9)}$$

It is interesting to note that Wilhelm Wien formulated (2.2.9) from empirical data in 1893. This was prior to the introduction of (2.2.5) in 1913[10] by his colleague, Maxwell Planck.

Wien's displacement law is represented below in Figure 2.2.3.

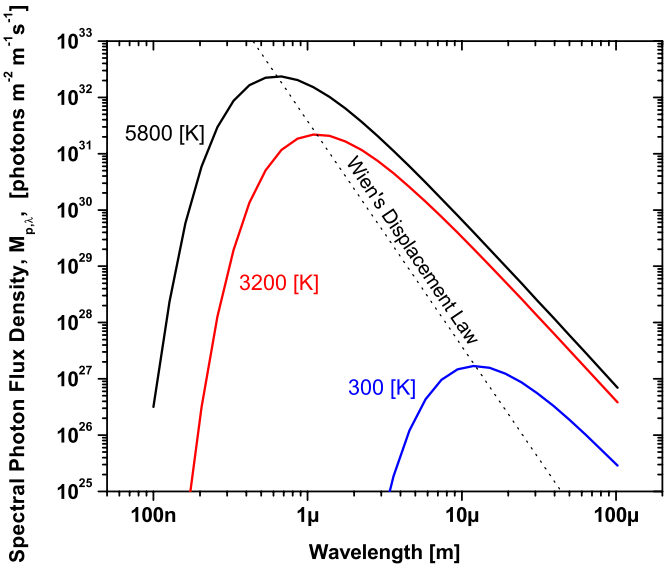

Figure 2.2.3 Planck's black body photon distribution for multiple temperatures with Wien's displacement law superimposed.

Therefore, combining equations (2.2.4), (2.2.8) and (2.2.9) results in a simple relationship for $SNR_{photon\ max}$ as a function of black body temperature, instrument spectral resolution, detector area, and measurement bandwidth.

$$SNR_{photon\ \max} = \sqrt{\frac{T_{BB}{}^4 \pi c \Delta\lambda_{res} A_d}{k_{Wien}{}^4 (e^{\frac{hc}{k_{Wien}k}} - 1)\Delta f}} = \sqrt{\frac{k_1 T_{BB}{}^4 \Delta\lambda_{res} A_d}{\Delta f}} \qquad \textbf{(2.2.10)}^1$$

Where k_1 is a constant.

(2.2.10) is more appropriately considered for resolution in optical frequency units, ($\Delta\nu_{res}$ [Hz]). Resolution in terms of optical frequency is transferable across the electromagnetic

[1] These equations neglect the Boson factor[5] which results in an $SNR_{photon\ max}$ error of < 1.0% for the assumptions in this thesis.

spectrum. Wavelength resolution, on the other hand, requires a conversion to optical frequency to be considered at different locations in the electromagnetic spectrum.

Therefore, using the known relationship between optical frequency and wavelength, combined with Wien's displacement law:

$$\Delta\nu_{res} = \frac{c}{\lambda_{\max}^{\ 2}}\Delta\lambda_{res} = \frac{cT_{BB}^{\ 2}}{k_{Wien}^{\ 2}}\Delta\lambda_{res} \qquad \textbf{(2.2.11)}$$

Where $\Delta\nu_{res}$ [Hz] is spectral resolution for one resolution element in optical frequency. Using (2.2.11), (2.2.10) becomes:

$$SNR_{photon\max} = \sqrt{\frac{k_2 T_{BB}^{\ 2}\Delta\nu_{res}A_d}{\Delta f}} \qquad \textbf{(2.2.12)}$$

Where k_2 is a constant.

(2.2.12) represents the maximum signal to noise ratio one can realize when detecting a scanned wavelength thermal emitter with a noiseless detector considering only photon noise. This limit cannot be realized because all photons from the black body cannot be collected and real detectors are not noiseless. Also, it is instructive to note that for real detectors, bandwidth decreases with area. This relationship, among others, is not considered here. However, (2.2.12) is a useful fundamental tool for evaluating real world systems with different specifications. The above analysis is similar to background limited infrared photodetector normalized detectivity, D^*_{BLIP} [cm $Hz^{1/2}$ W^{-1}], which is published by photodetector manufacturers. One can arrive at (2.2.12) using D^*_{BLIP} as shown in Appendix IV, though the derivation is less direct than the approach above.

Section 2.3 Beating Noise

The previous section treats noise associated with the statistical distribution of incident photons from a black body radiator per unit area and time. Here the noise associated with the interference of thermal light, or beating noise, is discussed. As will be seen, this noise is a function of spectral bandwidth of the light as well as detection bandwidth.

In general, thermal emitters, like the theoretical black body, radiate light at many different optical frequencies (wavelengths) as shown in Figure 2.2.2. Other attributes of thermal light are random polarization (unpolarized) and random phase (incoherent). A result of the random phase is that the light waves have an influence on one another. That is to say, waves interference both constructively and destructively with other waves because of phase differences. The result of this interaction is seen as beating noise at the detector.

The beating of polychromatic light was investigated both theoretically and experimentally by Walewski et al in [11]. In their work, Walewski et al relate the dependence of relative standard deviation[2] of light power measured to spectral bandwidth ($\Delta\nu_{res}$ [Hz]) and measurement bandwidth (Δf [Hz]) following the approach of Goodman[12]. Below is the relationship from [11] for unpolarized light with a Lorentzian spectral profile cast as beating signal-to-noise ratio (SNR_{beat} [-]).

[2] Signal-to-noise is the inverse of relative standard deviation

$$SNR_{beat} = \sqrt{\frac{2}{\frac{\Delta f}{\Delta \nu_{res}} + 0.5\left(\frac{\Delta f}{\Delta \nu_{res}}\right)^2\left(\exp\left(\frac{-2\Delta \nu_{res}}{\Delta f}\right)-1\right)}} \qquad \textbf{(2.3.1)}$$

As will be seen below, (2.3.1) can be approximated for extreme ratios of $\Delta\nu_{res}/\Delta f$.

$$SNR_{beat} \cong \begin{cases} \sqrt{\frac{2\Delta \nu_{res}}{\Delta f}} & for \ \frac{\Delta \nu_{res}}{\Delta f} > 10 \qquad \textbf{(2.3.2)} \\ \sqrt{2} & for \ \frac{\Delta \nu_{res}}{\Delta f} < 0.1 \qquad \textbf{(2.3.3)} \end{cases}$$

The complete equation for SNR_{beat} and its asymptotes are plotted in Figure 2.3.1.

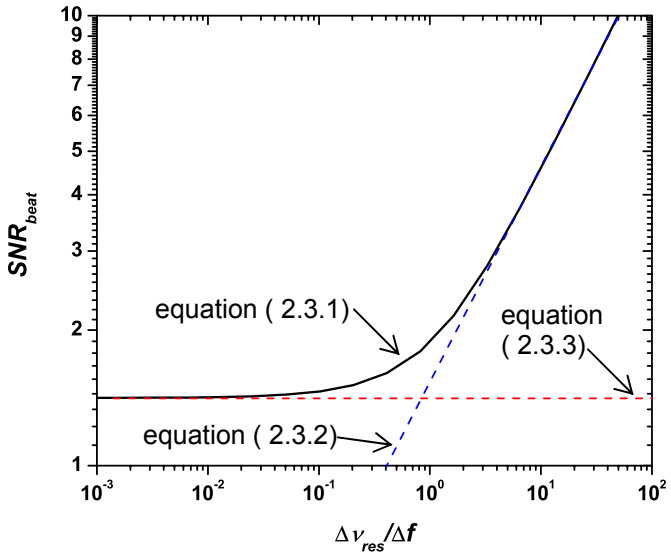

Figure 2.3.1 Optical beating noise limited *SNR* for unpolarized light with a Lorentzian spectral envelope as a function of spectral resolution ($\Delta\nu_{res}$ [Hz]) and measurement bandwidth (Δf [Hz]). The exact solution (2.3.1) is shown with the two asymptotes (2.3.2) and (2.3.3).

In general, it is seen from Figure 2.3.1 that SNR_{beat} is reduced when the measurement spectral resolution is increased (smaller $\Delta \nu_{res}$) and when the measurements are performed more quickly (larger Δf).

In closing the discussion of beating noise, an important finding by Walewski et al [11] should be stated. It was noted that SNR_{beat} is independent of total irradiance, meaning that increasing the power (or the number of photons), does not increase SNR_{beat}. This is in contrast to photon noise and many other noise sources considered by spectroscopists.

Section 2.4 Combined Photon and Beating Noise

Here photon and beating noise are combined resulting in an aggregate relationship useful for evaluating real systems. The two noise sources will be combined using the root sum squared (RSS) method which is appropriate for uncorrelated noise sources. However, since *SNR* is the inverse of the respective relative standard deviations, their reciprocals are involved. The following is the combination of the considered noise sources which results in the maximum signal-to-noise ratio, SNR_{max} [-].

$$SNR_{\max} = (SNR_{photon\max}{}^{-2} + SNR_{beat}{}^{-2})^{-0.5} \qquad \textbf{(2.4.1)}$$

Section 2.5 Summary and Comparison with Experiments

At this point it is instructive to combine (2.2.12) and (2.3.1) using (2.4.1), the result being a standard for evaluating experiments carried out by the author. Although the experiments will be presented completely in Appendix I, Appendix II, and Appendix III; some relevant parameters are listed here.

Table 2.5.1 Experimental and calculated values for experiments completed by the author. The three sources involved were a thermal emitter (TE), external cavity diode laser (ECDL), and a supercontinuum (SC). Detector area (A_d), measurement bandwidth for one spectral resolution element (Δf), spectral resolution ($\Delta \nu_{res}$), and the single cycle *SNR* of the experiment ($SNR_{experimental}$) are from the experiments. SNR_{photon}, SNR_{beat}, and SNR_{max} are calculated from (2.2.12), (2.3.1), and (2.4.1) respectively using a 3200 [K] black body.

	Experimental				*Calculated*		
	A_d	Δf	$\Delta \nu_{res}$	$SNR_{experimental}$	$SNR_{photon\ max}$	SNR_{beat}	SNR_{max}
	[m^2]	[Hz]	[Hz]	[-]	[-]	[-]	[-]
TE	6.3E-09	6.0E+03	8.8E+10	6	66344	5401	5383
ECDL	7.9E-07	4.0E+06	4.5E+10	20	20700	150	150
SC	3.1E-09	1.5E+08	1.6E+10	45	124	14	14

Table 2.5.1 contains values for experiments with three separate sources. Also listed in the table are *SNR* values calculated from the previously defined equations for each experimental source. This was done for comparison by treating the experimental sources

as if they were all black bodies at temperature of 3200 [K]. This temperature was the "color temperature" of the TE experiment (Appendix II) where the actual emissivity was 0.27 [-] over the spectral range of interest.

It is seen in the calculated values of Table 2.5.1 that SNR_{beat} is the lowest in all cases and therefore dominates SNR_{max}. Perhaps more interesting is the comparison between $SNR_{experimental}$ and SNR_{max} for each experiment. This comparison is shown graphically below.

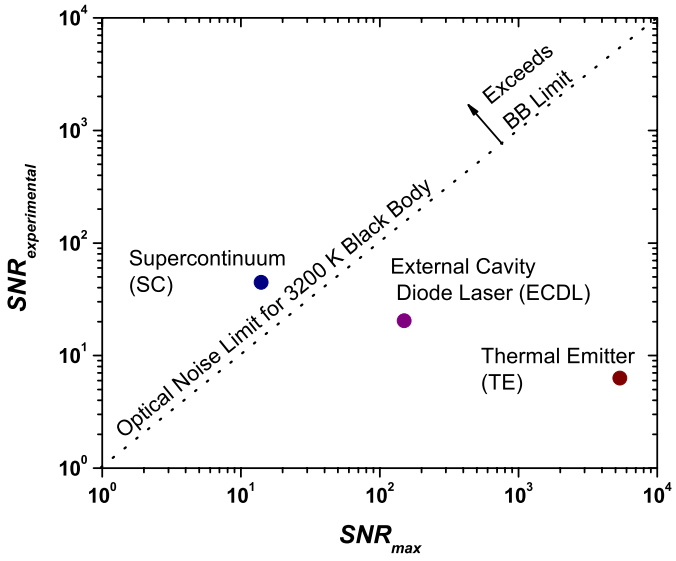

Figure 2.5.1 Comparison between SNR_{max} which is the maximum black body *SNR* calculated using the experimental A_d, Δf, $\Delta \nu_{res}$, and T_{BB} = 3200 [K] , and the experimental single cycle *SNR* ($SNR_{experimental}$).

It is seen in Figure 2.5.1 that the TE calculated maximum *SNR* was > 5000 whereas the actual was < 10. In this case it is believed that photon noise played a larger role in the actual experiment because of practical measurement considerations. These

considerations include an emissivity of less than one, collecting only a fraction of the emitter cone angle (solid angle), and poor optical system throughput.

On the other hand, the ECDL $SNR_{experimental}$ is much closer to the black body optical noise limit than the TE $SNR_{experimental}$. This is because the ECDL is a laser source and therefore has higher irradiance which effectively increases $SNR_{photon\ max}$. Additionally, the ECDL has a higher level of coherence than a TE which increases SNR_{beat}.

The ECDL experiment was an improvement with respect to the black body metric. However, it is seen in Figure 2.5.1 that the SC $SNR_{experimental}$ exceeds the black body limit for its detector area, bandwidth, and spectral resolution. Again, this is possible because of higher irradiance and coherence relative to the TE.

Note that in the actual measurements, single cycle data was taken over hundreds of cycles. The data was averaged for final *SNR*s much higher than $SNR_{experimental}$ in Table 2.5.1. Also, there are several real measurement factors which affected the three examples during collection which are not mentioned above. Some of these factors are listed below.

- Noise contributions of the detectors (e.g., Johnson noise).
- Noise contributions of the data acquisition system (e.g., bit noise).
- Mode noise from the combination of multimode collection fibers, window fouling, and beamsteering.

Additionally, although the SC looks like a good choice in the analysis above, there are drawbacks to absorption measurements using SC sources. For example, chirped light SC based experiments can exhibit a low frequency variation in the collected spectrum, or baseline instability. One source of this instability is fluctuation in the laser pump energy on the timescale of the experiment. An example of poor SC baseline performance can be seen in Appendix III. Another drawback to SC sources is with respect to spatial spectral dispersion and polarization. SC sources are polarized and are in general dispersed spatially by a polarization sensitive component such as a diffraction grating. Therefore, if the light polarization is changed upstream of the grating (for example, by transmission through a vibrating fiber optic cable) the result is a fluctuation in the collected signal. Additional detail regarding SC sources and polarization issues is given in Appendix II.

Chapter 3 Absorption Measurement Considerations

Section 3.1 Introduction

In this chapter a relationship between detector area and detection bandwidth is presented. This relationship is used to reduce the number of inputs to the photon noise equation. Also, the equation coupling *SNR* and *MDA* is introduced followed by a discussion on instrument broadening. The topics mentioned above increase the utility of the equations from the previous chapter for absorption measurements.

Section 3.2 Detector Area versus Bandwidth

Although there are several different photodetector technologies, one general trend is that the frequency response of the detector is a function of detector area. This relationship can be described as an RC circuit for a photodiode without voltage bias as:

$$\Delta f = \frac{1}{2\pi RC} \qquad \textbf{(3.2.1)}$$

Where Δf [Hz] is the detector frequency response, R[Ω] is the resistive load, and C[F] is the detector capacitance. Since C can be described in capacitance per unit area A for a given material, (3.2.1) can be interpreted as:

$$\Delta f = \frac{1}{2\pi R \frac{C}{A} A_d} \qquad \textbf{(3.2.2)}$$

This relationship is described by Dereniak and Boreman [4] for 50 [Ω] germanium (Ge) detectors as:

$$\Delta f = \frac{k_3}{A_d} \qquad \textbf{(3.2.3)}$$

(3.2.3) is plotted with empirical data for both indium gallium arsenide (InGaAs) detectors and long wave InGaAs detectors in Figure 3.2.1.

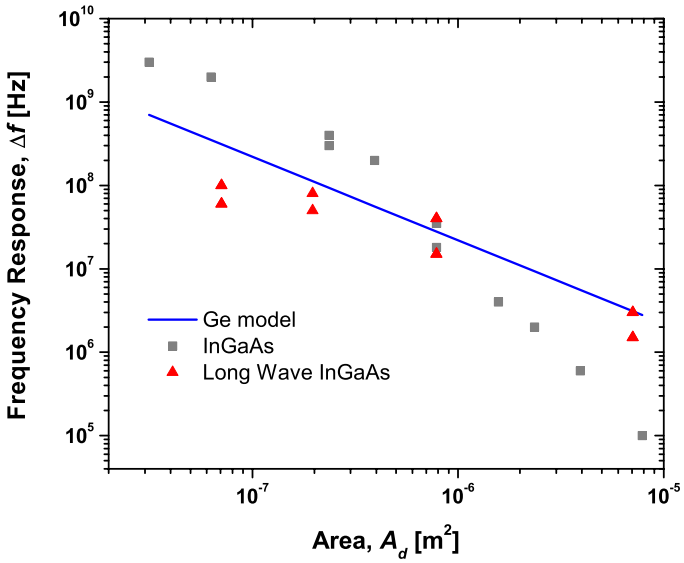

Figure 3.2.1 Photodetector frequency response dependence on area for both the 50 Ω germanium (Ge) model and empirical InGaAs photodetector specifications (source: Hamamatsu).

In Figure 3.2.1 the detector frequency response dependence on area is obvious for both the model and the empirical data. However, we can see that each data set has a slightly different slope due to material properties (i.e., different values of C/A).

From this point forward, (3.2.3) will be used to relate Δf to A_d. That is, the measurement bandwidth and detector area relationship for a germanium photodetector will be assumed in all cases. As a result, (3.2.3) can be combined with (2.2.12) to remove the dependence of $SNR_{photon\ max}$ on detector area.

$$SNR_{photon\ \max} = \sqrt{\frac{k_4 {T_{BB}}^2 \Delta \nu_{res}}{\Delta f^2}} \qquad \textbf{(3.2.4)}$$

Section 3.3 Signal-to-Noise Ratio to Minimum Detectable Absorbance

Although *SNR* is a useful metric for comparing measurement systems, minimum detectable absorbance (*MDA*) is a useful analogue to *SNR* in spectroscopy. That is to say, it is useful for a spectroscopist to think in terms of the lowest level of absorbance which can be detected in an experiment. In this section a relationship between *SNR* and *MDA* is developed using the example absorption line shown in Figure 3.3.1 below.

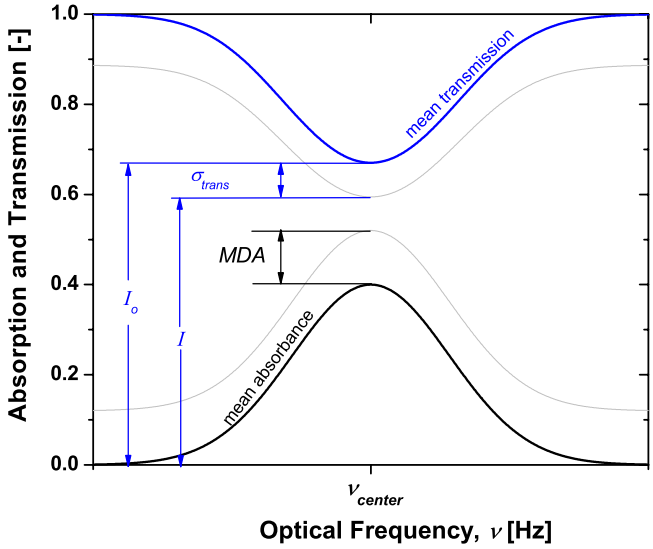

Figure 3.3.1 Example absorption line (Gaussian) plotted with the corresponding transmission. Where I_o is the noiseless transmission, σ_{trans} is the transmission uncertainty, I is the transmission attenuated by the uncertainty amount, and MDA is the minimum detectable absorbance.

Figure 3.3.1 can be used with the Beer-Lambert relationship to develop the equation below.

$$\frac{I}{I_o} = \frac{\overline{trans} - \sigma_{trans}}{\overline{trans}} = 1 - \frac{\sigma_{trans}}{\overline{trans}} = 1 - \frac{1}{SNR} = \exp(-MDA) \qquad \textbf{(3.3.1)}$$

Where I_o [-] is the noiseless transmission, I [-] is the transmission attenuated by the transmission uncertainty, $\overline{trans}$ [-] is the mean transmission, σ_{trans} [-] is the transmission uncertainty, and MDA [-] is the minimum detectable absorbance.

(3.3.1) is solved for SNR here:

$$SNR = \frac{1}{1 - \exp(-MDA)} \qquad \textbf{(3.3.2)}$$

A useful approximation of (3.3.2) is:

$$SNR \approx \frac{1}{MDA} \qquad \textbf{(3.3.3)}$$

The use of (3.3.3) to approximate (3.3.2) results in < 5 [%] error in *SNR* for an *MDA* < 0.1. However, the error in *SNR* from using (3.3.3) increases linearly with *MDA* as shown in Figure 3.3.2.

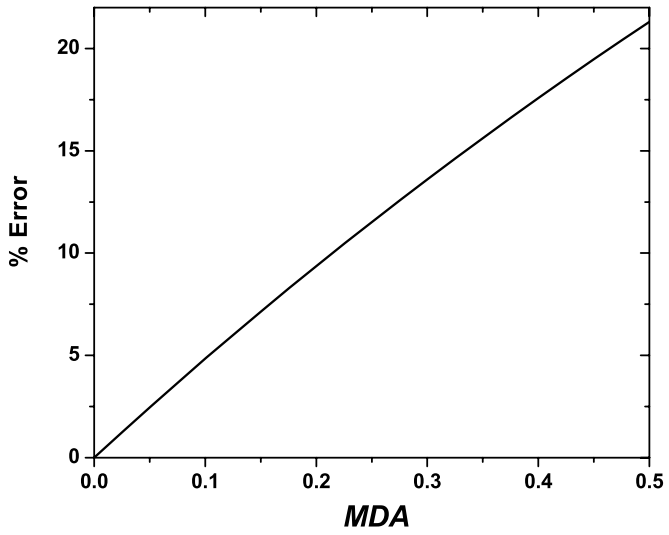

Figure 3.3.2 Error in calculating SNR_{max} using the approximate relationship (3.3.3).

Section 3.4 Instrument Broadening

SNR as a function of *MDA* was developed in the previous section using the example absorption line in Figure 3.3.1. This example is appropriate if the absorption feature is fully resolved, meaning the instrument spectral resolution is better than the absorption

feature full width at half maximum (FWHM or $\Delta\nu_{feature}$). However, as instrument resolution degrades, the measured absorption feature broadens and the height is lowered (i.e., area is conserved). The result of this broadening is a decrease in *MDA* and therefore an increase in the required *SNR*.

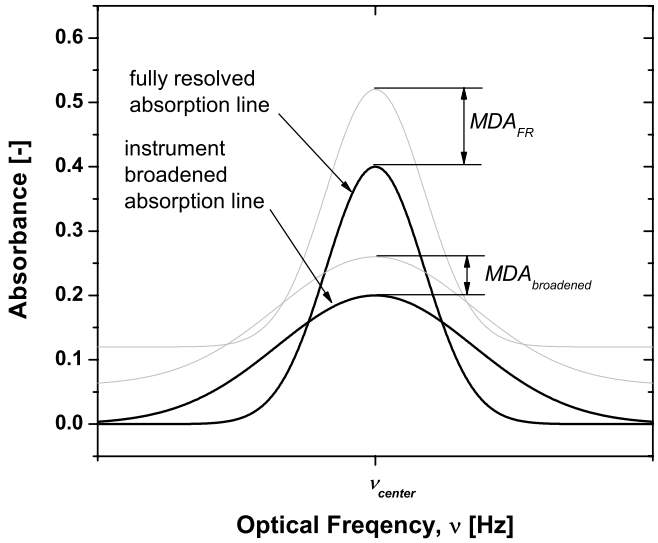

Figure 3.4.1 The effect of instrument broadening on *MDA*. The fully resolved *MDA* (MDA_{FR}) is reduced to $MDA_{broadened}$ as the line width is increased.

The effect of instrument broadening on *MDA* is obvious in Figure 3.4.1. This effect is described for the convolution of two Gaussian lineshapes in equation form below[13].

$$MDA_{broadened} = \frac{MDA_{FR}}{\sqrt{1+\frac{\Delta\nu_{res}^{\ 2}}{\Delta\nu_{feature}^{\ 2}}}} \qquad \textbf{(3.4.1)}$$

Where $MDA_{broadened}$ [-] is the instrument broadened *MDA*, MDA_{FR} [-] is the fully resolved *MDA*, $\Delta\nu_{feature}$ [Hz] is the fully resolved absorption feature full width at half maximum, and $\Delta\nu_{res}$ [Hz] is the spectral measurement resolution.

The influence of instrument broadening on both *MDA* and *SNR* are illustrated in Figure 3.4.2 below.

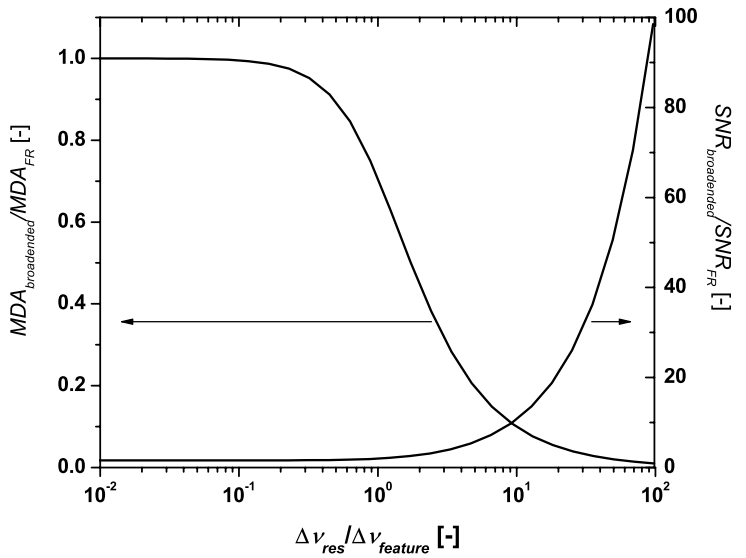

Figure 3.4.2 Influence of instrument broadening on both *MDA* and *SNR*.

Figure 3.4.2 is best explained by an illustration. For example, say one wishes to measure an absorption feature which is 10E+10 [Hz] wide ($\Delta\nu_{feature}$) with a sensitivity of 0.01 [-] (MDA_{FR}) using an instrument with a resolution of 100E+10 [Hz] ($\Delta\nu_{res}$). The *SNR* necessary to measure the fully resolved feature is ~100 [-] (SNR_{FR}) from (3.3.2). However, it is seen from Figure 3.4.2 that instrument broadening ($\Delta\nu_{res}/\Delta\nu_{feature} = 10$)

decreases the *MDA* to ~0.001 ($MDA_{broadened}$). Therefore, the required *SNR* for the measurement system becomes ~1000 ($SNR_{broadened}$). In this example it is shown that instrument broadening can play a significant role in the final specification of *SNR* when spectrally under-resolved equipment is used.

Section 3.5 Summary

A simple relationship for detection bandwidth and detection area was introduced in this chapter. Also, it was seen that *SNR* can be related to *MDA*. Finally, the effect of the instrument broadening was detailed. In the next chapter the equations above will be used to evaluate real experiments.

Chapter 4 Applied Calculations

Section 4.1 Introduction

In this chapter the equations developed above will be used to calculate thermal-emitter optical-noise limits. The input values for the calculations will be similar to the measurement specifications from the H_2O and H_2O_2 experiment included in Appendix I. This chapter will progress as follows. First, specifications are calculated for a H_2O measurement using both chirped light and spatial spectral dispersion. Second, the calculations are repeated for H_2O_2. Third, the combined measurement of H_2O and H_2O_2 is considered. The chapter concludes with a table summarizing the results and a brief discussion.

Section 4.2 H_2O Measurement Using Chirped Light

In this chapter's first example, a chirped light arrangement (Figure 2.2.1a) will be consider. The goal is to determine the systems specifications necessary to measure crank angle resolved absorption spectra of the $\nu_1 + \nu_3$ combination band of H_2O in the HCCI engine referred to in Appendix I. The engine is running at 600 [RPM] and it is desirable to collect one complete spectrum for each crank angle degree (*CAD*). A measurement collected every *CAD* is termed a "crank-angle-resolved measurement". For this example, the engine speed dictates a crank-angle-resolved spectral collection rate of 3600 [Hz] (one spectrum every 278 [μs]).

Using the known engine geometry and operating conditions, we can obtain approximate in-cylinder thermodynamic properties using a chemical kinetics modeling package (CHEMKIN). The in-cylinder properties for this engine prior to primary heat release (precombustion) are a temperature of ~900 [K] , a pressure of ~20 [bar], and a H_2O mole fraction of ~0.01. Precombustion conditions are chosen because the measurement requirements are challenging at low pressures and low H_2O mole fractions.

Proceeding with the information from the CHEMKIN model, a simulated H_2O absorption spectra can be retrieved from the HITRAN spectral database[14].

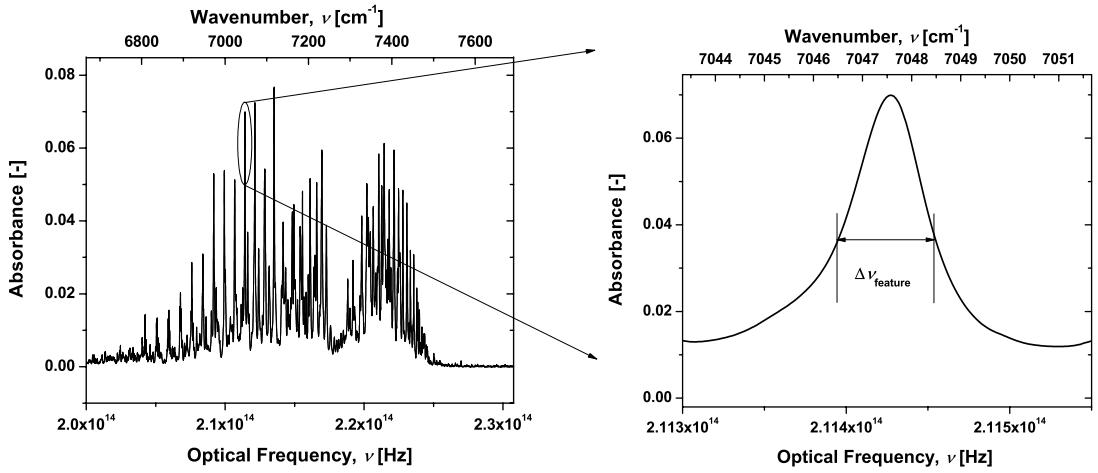

Figure 4.2.1 Simulated fully-resolved absorption spectrum from HITRAN for the $\nu_1 + \nu_3$ combination band of H_2O at 900 [K], 20 [bar], 0.01 mole fraction, and an optical path length of 0.1 [m]. Also included is a zoom of a representative absorption feature with a FWHM or $\Delta\nu_{feature}$ equal to ~6E10 [Hz] (~2 [cm^{-1}]).

A majority of the fully resolved H_2O features for the stated engine conditions reside in the 2.00E+14 - 2.31E+14 [Hz] (6667-7692 [cm^{-1}]) range shown in Figure 4.2.1. This range defines the desired spectral coverage of the measurement or $\Delta\nu_{total}$ (~3.1E+13 [Hz], ~1000 [cm^{-1}]) which will remain constant throughout this chapter. Also, the maximum absorption in Figure 4.2.1 is ~0.08 [-] from which it is decided to measure within ~13 [%] uncertainty setting the fully resolved minimum detectable absorbance at 0.01[-] (MDA_{FR}). The uncertainty for this example was chosen arbitrarily. In general, the acceptable uncertainty in an absorption measurement is related to the type of post processing for which the data is intended. For instance, data collected for qualitative absorption

measurements can have more relaxed uncertainties than data collected for quantitative measurements.

The last important piece of information in Figure 4.2.1 is in the zoomed plot. In this plot a representative line of the absorption band has been selected in order to quantify the features fully resolved spectral width ($\Delta\nu_{feature}$), which is as ~6E+10 [Hz].

Before assembling the relevant *SNR* equations, it is important to recognize the following relationship for chirped light measurements.

$$\Delta\nu_{res}\Delta f = \left(\frac{\Delta\nu_{total}}{\#_{res\,elements}}\right)\left(\Delta f_{total}\,\#_{res\,elements}\right) = \Delta\nu_{total}\Delta f_{total} \qquad \textbf{(4.2.1)}$$

Where $\Delta\nu_{res}$ [Hz] is the spectral resolution, Δf [Hz] is the measurement bandwidth, $\Delta\nu_{total}$ [Hz] is the spectral range of the measurement, Δf_{total} [Hz] is the bandwidth for measuring $\Delta\nu_{total}$, and $\#_{res\ elements}$ [-] is the number of resolution elements over the spectral range. This relationship is essentially the definition of the single quantities $\Delta\nu_{res}$ and Δf in terms of their summations over the number of elements observed while measuring a spectrum.

Therefore, using the relationship developed above and the Engineering Equation Solver (EES) software, we can solve for the optical noise limited specifications of the proposed measurement using the same black body temperature as in Section 2.5. A table of the relevant equations for the example in this section is shown below. Also below are the tabulated inputs for this example, which were described in the beginning of this section, and the calculated results.

Table 4.2.1 Equations for chirped light H_2O absorption measurements for Section 4.2 example.

EQUATION	NUMBER	PAGE
$\Delta\nu_{res}\Delta f = \Delta\nu_{total}\Delta f_{total}$	(4.2.1)	31
$SNR_{photon\,\max} = \sqrt{\frac{k_4 T_{BB}{}^2 \Delta\nu_{res}}{\Delta f^2}}$	(3.2.4)	22
$SNR_{beat} = \sqrt{\frac{2}{\frac{\Delta f}{\Delta\nu_{res}} + 0.5\left(\frac{\Delta f}{\Delta\nu_{res}}\right)^2\left(\exp\left(\frac{-2\Delta\nu_{res}}{\Delta f}\right)-1\right)}}$	(2.3.1)	14
$SNR_{\max} = (SNR_{photon\,\max}{}^{-2} + SNR_{beat}{}^{-2})^{-0.5}$	(2.4.1)	15
$SNR_{\max} = \frac{1}{1-\exp(-MDA_{broadened})}$	(3.3.2)	23
$MDA_{broadened} = \frac{MDA_{FR}}{\sqrt{1+\frac{\Delta\nu_{res}{}^2}{\Delta\nu_{feature}{}^2}}}$	(3.4.1)	25

Table 4.2.2 Equation inputs and results for H_2O measurement using chirped light.

INPUTS		RESULTS	
MDA_{FR}	0.01 [-]	Δf	4.320E+06 [Hz]
$\Delta\nu_{feature}$	6E+10 [Hz]	$\Delta\nu_{res}$	2.584E+10 [Hz]
Δf_{total}	3600 [Hz]	$MDA_{broadened}$	0.009185 [-]
$\Delta\nu_{total}$	3.1E+13 [Hz]	SNR_{photon}	38355 [-]
T_{BB}	3200 [K]	SNR_{beat}	109.4 [-]
		SNR_{max}	109.4 [-]

We see from Table 4.2.2 that the initial specifications can be met by a black-body noiseless-detector combination with reasonable detection bandwidth (4.3 [MHz]) and spectral resolution (~26 [GHz] or ~0.9 [cm^{-1}]). Also, beating noise is the primary noise contributor. However, although SNR_{photon} is >> SNR_{beat} in this example, SNR_{photon} can be expected to be significantly reduced for an actual measurement due to practical optics limitations as mentioned in Section 2.5.

Section 4.3 H_2O Measurement Using Spatial Spectral Dispersion

The exercise from Section 4.2 is repeated here for the spatial spectral dispersion arrangement (Figure 2.2.1b). The inputs here are the same as Section 4.2 with the exception that $\Delta\nu_{total}$ is no longer necessary because $\Delta\nu_{total}$ is a function of the number of photodetectors (pixels) one chooses to use. The same equation set as Table 4.2.1 is used here with the exception that (4.2.1) is replaced with the equation below.

$$\Delta f = \Delta f_{total} \qquad \textbf{(4.3.1)}$$

The inclusion of (4.3.1) is a result of all pixel elements of an array detector being integrated simultaneously. The results for the slightly modified set of equations are given below.

Table 4.3.1 Equation inputs and results for H_2O measurement using spatial spectral dispersion.

INPUTS		RESULTS	
MDA_{FR}	0.01 [-]	Δf	3600 [Hz]
$\Delta \nu_{feature}$	6E+10 [Hz]	$\Delta \nu_{res}$	1.818E+07 [Hz]
Δf_{total}	3600 [Hz]	$MDA_{broadened}$	0.01 [-]
$\Delta \nu_{total}$	NA	SNR_{photon}	1.221E+06 [-]
T_{BB}	3200 [K]	SNR_{beat}	100.5 [-]
		SNR_{max}	100.5 [-]

The drastic reduction in the required measurement bandwidth from 4.320E+06 [Hz] to 3600 [Hz] as a result of (4.3.1) is reflected in both the large increase in SNR_{photon} and an increase in the achievable instrument resolution (~20 [MHz] or 0.0006 [cm^{-1}]). Note that to implement this resolution over the $\Delta \nu_{total}$ would require dispersing the light over > 1E+6 pixels. This may not be practical because of grating limitations and linear array manufacturing limitations.

Section 4.4 H_2O_2 Measurement Using Chirped Light

In Section 4.2 and Section 4.3 H_2O measurements similar to Appendix I were investigated. In this section the chirped light measurement calculations from Section 4.2 are repeated for H_2O_2, which is also similar to Appendix I. The equation set here is identical to Table 4.2.1. However, there are two differences in the input variables. First,

H_2O_2 is a broad absorber and therefore the $\Delta\nu_{feature}$ will increase. For this example, $\Delta\nu_{feature}$ will be increased from 6E+10 to 6E+12 [Hz] (from ~2 to ~200 [cm^{-1}]). Second, H_2O_2 is less abundant than H_2O and does not absorb as strongly over the selected wavelength range, resulting in a decrease in MDA_{FR}. MDA_{FR} will be decreased from 0.01 to 0.001 for the H_2O_2 example. The relative absorption characteristics of H_2O_2 and H_2O are shown schematically below.

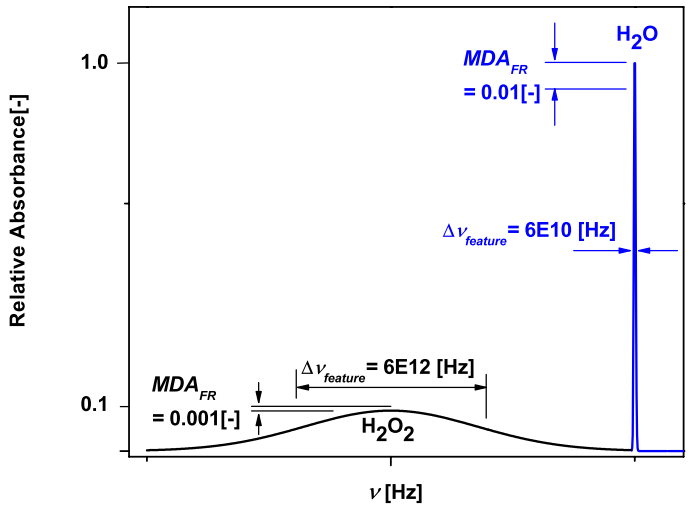

Figure 4.4.1 Example absorption features for H_2O_2 and H_2O. Note that in the real experiments detailed in Appendix I these features overlap in the actual measurement, but are separated here for clarity.

The results for the chirped light measurement of H_2O_2 are shown below.

Table 4.4.1 Equation inputs and results for H_2O_2 measurement using chirped light.

INPUTS		RESULTS	
MDA_{FR}	0.001 [-]	Δf	471636 [Hz]
$\Delta \nu_{feature}$	6E+12 [Hz]	$\Delta \nu_{res}$	2.365E+11 [Hz]
Δf_{total}	3600 [Hz]	$MDA_{broadened}$	0.0009992 [-]
$\Delta \nu_{total}$	3.1E+13	SNR_{photon}	1.062E+06 [-]
T_{BB}	3200 [K]	SNR_{beat}	1001 [-]
		SNR_{max}	1001 [-]

We see from the results above that the relaxation of the $\Delta \nu_{feature}$ requirement dominates the decrease in MDA_{FR} as far as the measurement bandwidth and spectral resolution are concerned. Both the measurement bandwidth (~500 [kHz]) and the spectral resolution (~230 [GHz] or ~8 [cm^{-1}]) are achievable values.

Section 4.5 H_2O_2 Measurement Using Spatial Spectral Dispersion

The set of inputs and equations used in Section 4.3 are used here with the input values from Section 4.4 for a spatial spectral dispersion measurement of H_2O_2. The results are below.

Table 4.5.1 Equation inputs and results for H_2O_2 measurement using spatial spectral dispersion.

INPUTS		RESULTS	
MDA_{FR}	0.001 [-]	Δf	3600 [Hz]
$\Delta \nu_{feature}$	6E+12 [Hz]	$\Delta \nu_{res}$	1.802E+09 [Hz]
Δf_{total}	3600 [Hz]	$MDA_{broadened}$	0.001 [-]
$\Delta \nu_{total}$	NA	SNR_{photon}	1.215E+07 [-]
T_{BB}	3200 [K]	SNR_{beat}	1001 [-]
		SNR_{max}	1001 [-]

Again we see that the reduced measurement bandwidth requirement of the spatial spectral dispersion case results in the possibility of measuring with a high spectral resolution (~2 [GHz] or ~0.06), as in Section 4.3. However, the H_2O_2 feature is broad (6 [THz] or 200 [cm^{-1}]) and therefore the high resolution is not necessary.

This measurement could be made with a reasonable number of pixels over the measurement range (~2E+4 in contrast to > 1E+6 in Section 4.3). As an example, the measurement in Appendix II was made with a linear array detector with > 1E+3 pixels, only a factor of 20 lower than the number of pixels required here.

Section 4.6 H_2O and H_2O_2 Measurement Using Chirped Light

Here the set of equations from Table 4.2.1 is used to measure H_2O and H_2O_2 simultaneously. This multispecies measurement will require the feature resolution of 6E+10 [Hz] from H_2O and the fully resolved minimum detectable absorbance of 0.001 from H_2O_2.

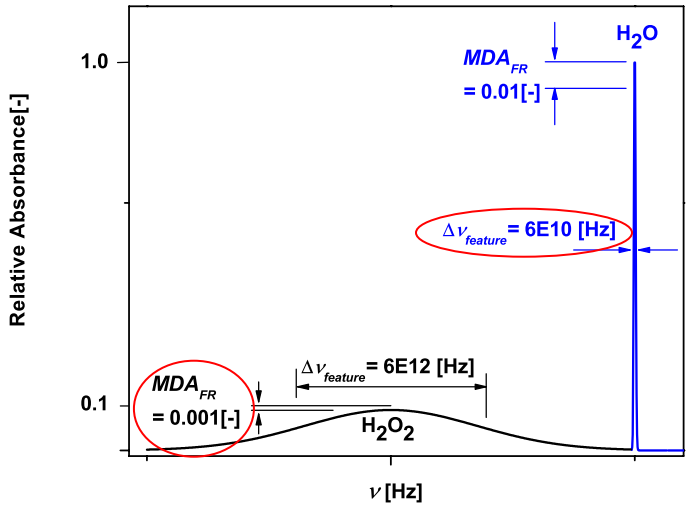

Figure 4.6.1 Absorption features plot with input values for Section 4.6 highlighted.

It is seen in Figure 4.6.1 that the combined H_2O and H_2O_2 measurement will require both high spectral resolution and absorption sensitivity. The table of inputs and results are shown below.

Table 4.6.1 Equation inputs and results for combined H_2O and H_2O_2 measurement using chirped light.

INPUTS		RESULTS	
MDA_{FR}	0.001 [-]	Δf	No solution
$\Delta \nu_{feature}$	6E+10 [Hz]	$\Delta \nu_{res}$	
Δf_{total}	3600 [Hz]	$MDA_{broadened}$	
$\Delta \nu_{total}$	3.1E+13	SNR_{photon}	
T_{BB}	3200 [K]	SNR_{beat}	
		SNR_{max}	

It is seen in Table 4.6.1 that the system of equations could not be solved for numerical results. Therefore, the equations were solved repeatedly for the inputs in Table 4.6.1, where $\Delta \nu_{feature}$ was varied from 6E12 to 6E10 [Hz]. The results of the parametric calculations are shown below.

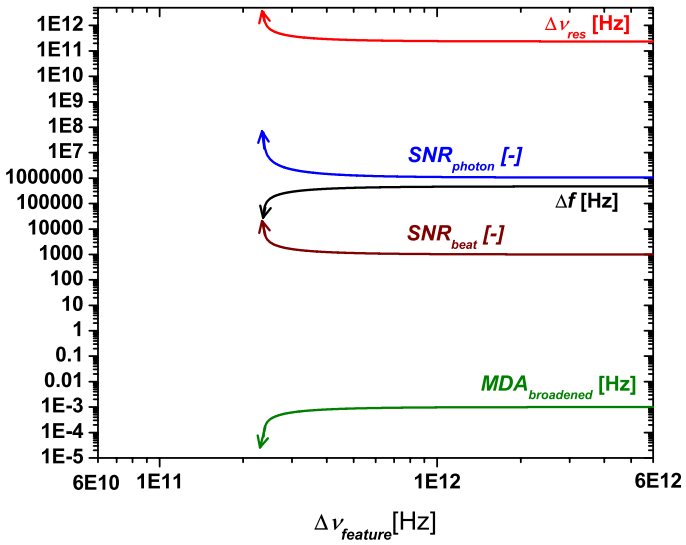

Figure 4.6.2 Calculation results for all output variables for decreasing feature resolution ($\Delta\nu_{feature}$) with all other inputs from Table 4.6.1 held constant.

It is apparent from Figure 4.6.2 that the equation set cannot be solved for $\Delta\nu_{feature}$ equal to 6E+10 [Hz]. That is, all output variables are approaching either positive infinity or zero near 2.3E+11 [Hz]. The extreme behavior of the data in Figure 4.6.2 at decreasing frequencies is due to the instrument broadening equation (3.4.1). In short, as $\Delta\nu_{feature}$ is decreased, $\Delta\nu_{res}$ is increased through other relationships. This continues without much consequence until $\Delta\nu_{res}/\Delta\nu_{feature} > 1$ after which instrument broadening becomes a significant factor as shown in Figure 3.4.2. Note that $\Delta\nu_{res}/\Delta\nu_{feature} < 1$ for all previous calculations in this chapter.

In general, the behavior in Figure 4.6.2 can be described as a limiting case where the spectrum has been broadened enough so that there is a measurement of only one spectral element per scan. This statement is shown in equation form below.

$$\Delta f = \Delta f_{total} \qquad \textbf{(3.2.1)}$$

$$\Delta \nu_{res} = \Delta \nu_{total} \qquad \textbf{(4.6.1)}$$

Using (3.2.1) and (4.6.1) with the equation set from Table 4.2.1 one can solve for a locus of points describing the limitations of sensing with thermal light. Furthermore, the input parameters can be organized into the comprehensive relationship shown below.

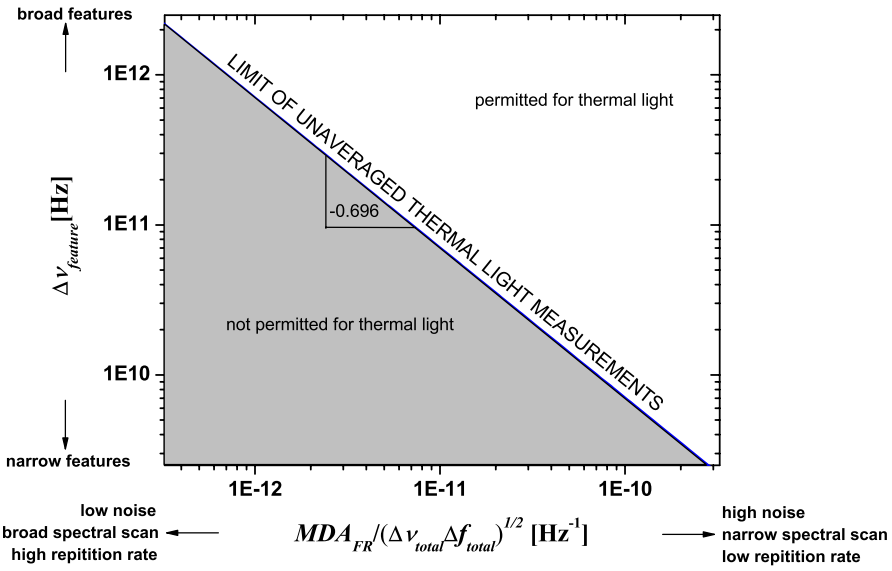

Figure 4.6.3 Limit for single cycle thermal light measurements where thermal beating is the dominant noise source, which is the case throughout this thesis.

It should be noted that Figure 4.6.3 does not take into account the influence of T_{BB}. However, we have seen that SNR_{max} is dominated by thermal beating which is

independent of the number of photons. Additionally, T_{BB} must be reduced below 40 [K] for there to be any change in Figure 4.6.3 considering the input parameters used in Section 4.2 (which is equivalent to ~0.01 [%] of the photons at 3200 [K]). Therefore, the reader is cautioned that Figure 4.6.3 is useful for theoretical limit calculations. But, for a real system with reduced optical throughput one must check that $SNR_{beat} >> SNR_{photon}$ before using Figure 4.6.3.

Section 4.7 H_2O and H_2O_2 Measurement Using Spatial Spectral Dispersion

In light of the lack of solution in the above, it is of interest to calculate the values for the same inputs for a spatial spectral dispersion measurement. The results are shown below.

Table 4.7.1 Equation inputs and results for combined H_2O and H_2O_2 measurement using spatial spectral dispersion.

INPUTS		RESULTS	
MDA_{FR}	0.001 [-]	Δf	3600 [Hz]
$\Delta \nu_{feature}$	6E+10 [Hz]	$\Delta \nu_{res}$	1.803E+09 [Hz]
Δf_{total}	3600 [Hz]	$MDA_{broadened}$	0.0009995 [-]
$\Delta \nu_{total}$	NA	SNR_{photon}	1.215E+07 [-]
T_{BB}	3200 [K]	SNR_{beat}	1001 [-]
		SNR_{max}	1001 [-]

It is seen in Table 4.7.1 that the system solves. Additionally, note that the results here are almost identical to the results in Section 4.5. The reason for the similarity between the two sections is that their equations are both driven primarily by the MDA_{FR} input and not by the $\Delta\nu_{feature}$. The lack of influence of $\Delta\nu_{feature}$ is again because $\Delta\nu_{res}/\Delta\nu_{feature} < 1$. However, it is interesting to note that this ratio is much closer to 1 in this section than in Section 4.5.

Section 4.8 Summary

In this chapter the equations developed earlier in the thesis were tested for several different scenarios involving H_2O and H_2O_2 measurements. A summary of the input variables and results are below.

Table 4.8.1 Summary of Chapter 4 calculations

		INPUTS		RESULTS			
Species	Spectral Disp.	MDA_{FR} [-]	$\Delta\nu_{feature}$ [Hz]	Δf [Hz]	$\Delta\nu_{res}$ [Hz]	$MDA_{broadened}$ [-]	SNR_{max} [-]
H_2O	chirped	0.01	6E+10	4.32E+06	2.58E+10	0.009185	109.4
H_2O	spatial	0.01	6E+10	3.60E+03	1.82E+07	0.01	100.5
H_2O_2	chirped	0.001	6E+12	4.72E+05	2.37E+11	0.0009992	1001.0
H_2O_2	spatial	0.001	6E+12	3.60E+03	1.80E+09	0.001	1001.0
H_2O H_2O_2	chirped	0.001	6E+10	No Solution			
H_2O H_2O_2	spatial	0.001	6E+10	3.60E+03	1.80E+09	0.0009995	1001.0

One conclusion to be drawn from these calculations is that instrument broadening can quickly force the results to unreasonable numbers. This was the case in Section 4.6 where the equation set could not be solved for the inputs when measuring with chirped light. Note that the inputs to Section 4.6 are very near the inputs for the experiment in Appendix I. It is apparent from this chapter that the measurement in Appendix I could not be made on a single cycle basis with a thermal emission source. Furthermore, the *SNR*s quoted are not realizable in a thermal emitter system because of practical constraints such as limited photon collection. Therefore, as with the work done in Appendix I, Appendix II, and Appendix III; averaging is employed to increase *SNR* for actual measurements. Roughly, *SNR* is increased by the root of the number averages. Likewise *MDA* is approximately decreased by the square root of the number of averages.

For instance, the equations for Section 4.6 solve easily for a $\Delta\nu_{feature}$ of 6E+12 [Hz] and a relaxed MDA_{FR} of 0.004. If the measurement were averaged over 16 engine cycles, the MDA_{FR} would decrease by a factor of 4 resulting in the originally requested 0.001.

More important than the instrument broadening is the fact that spatial spectral dispersion outperforms chirped light in all cases. This is because all elements are read at the same time which is equivalent to having many detectors reading slowly versus one detector collecting all of the information very quickly. As mentioned above, the practicality of spatially dispersing the light may be in question. However, as a rule, considering optical noise, one is best served by using spatial dispersion.

Chapter 5 Heisenberg Limited Detection of Thermal Light

Section 5.1 Introduction

A system of equations has been developed to characterize optical noise for transient photon detection of thermal emitters. It has been shown that these equations can be used to compare absorption systems with different light sources. Also, it has been shown that this system of equations can be useful as a pre-experiment check using the desired measurement criteria as in Appendix I. In this section absorption is set aside and the discussion moves back to SNR ratio only, as in Chapter 2. Next, a fundamental limit, the Heisenberg uncertainty principle, is employed as a metric for ultrafast high-spectral resolution detection of a thermal emitter. The developed relationship is then used to evaluate the experiments in Appendix I, Appendix II, and Appendix III.

Section 5.2 The Heisenberg Uncertainty Principle

The Heisenberg uncertainty principle was translated into English as the following statement:

> "The more precisely the position is determined, the less precisely the momentum is known in this instant, and vice versa." –Werner Heisenberg, 1927[15]

The quotation above can be cast into an energy time relationship as done by Silfvast[16] below.

$$\Delta E \Delta t \geq \frac{h}{2\pi} \quad \textbf{(5.2.1)}$$

Where ΔE [J] is the uncertainty in energy, Δt [s] is the uncertainty in time, and h [J-s] is Planck's constant. Next, (5.2.1) is recast and expanded below as an equality to designate experiments at the Heisenberg limit.

$$\Delta E \Delta t = h \Delta \nu_{res} \Delta t = \frac{h \Delta \nu_{res}}{\Delta f} = \frac{h}{2\pi} \quad \textbf{(5.2.2)}$$

Furthermore, by canceling h the equation reduces to:

$$\frac{\Delta \nu_{res}}{\Delta f} = \frac{1}{2\pi} = k_5 \quad \textbf{(5.2.3)}$$

(5.2.3) is the minimum ratio of spectral resolution to measurement bandwidth as determined by Heisenberg. That is, (5.2.3) constrains the resolution and speed by which any photonic measurement can be made. Using (5.2.3), a system of equations can be developed to solve for the maximum *SNR* possible for Heisenberg limited measurements of a thermal emitter at 3200 [K] by a noiseless-unbiased RC type photodetector. The combination of the photon noise equation (2.2.12), the beating noise equation (2.3.1), their summation (2.4.1), and Heisenberg uncertainty principle (5.2.3), results in the equation below.

$$SNR_{\max} = \sqrt{\frac{k_6}{\frac{\Delta f}{k_7} + 1}} \quad \textbf{(5.2.4)}$$

It is seen in the equation above that SNR_{max} becomes a function only of detection bandwidth, Δf [Hz]. This relationship is plotted below.

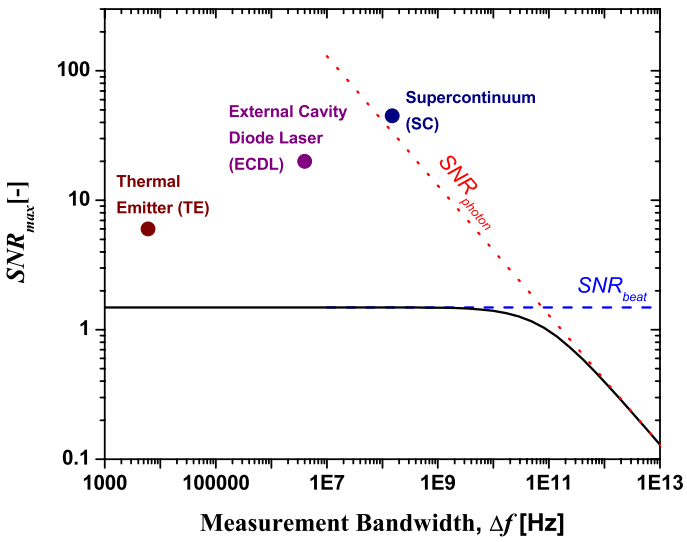

Figure 5.2.1 Maximum signal to noise ratio (SNR_{max}) for Heisenberg limited sensing of a thermal emitter, as a function of measurement bandwidth (Δf) only. The asymptotes are the photon noise (T_{BB} = 3200 [K]) and beating noise, respectively. Single cycle data for actual experiments: TE (Appendix II), ECDL (Appendix I), and SC (Appendix III), are also plotted for discussion.

Section 5.3 Summary

Although high speed and high resolution detection are desirable for highly transient phenomena, the repercussions of measuring thermal light with a Heisenberg limited instrument is seen in Figure 5.2.1. That is to say, thermal beating noise limits SNR_{max} to ~1.5 until frequencies are greater than ~1 [GHz] where it is degraded still further by

photon noise. Also, it is seen in Figure 5.2.1 that the actual experiments outperform the Heisenberg limited device because of their combination of low spectral resolution and low detection bandwidths.

Chapter 6 Summary and Conclusions

This thesis includes experimental (Appendix I, Appendix II, and Appendix III) and theoretical investigations by the author which improve the understanding of broad-wavelength absorption-spectroscopy as applied to combustion measurements. In the appendix, the author will show that experimental absorption spectra collected in an HCCI engine can exceed hundreds of nanometers in breadth, be collected in less than a millisecond, and have averaged absorption sensitivities (*MDA*) on the order of 0.1%. These experiments motivated a theoretical optical-noise analysis of broad-wavelength absorption-spectroscopy based on thermal emitters.

Thermal light was chosen as a basis for the model development because it is ubiquitous and consists of a broad continuous spectrum. The model was exercised using example calculations based on the author's experiments. Along with the calculated results, there were several other important conclusions. Specifically, beating noise dominated photon noise in the theoretical examples. Also, lasers can have lower optical noise than thermal emitters because they have higher coherence and higher irradiance. In addition, the dependence of spectral resolution on other specifications, such as *MDA*, can be characterized. Furthermore, spatial dispersion is preferred to chirped light based on their respective impact on collection bandwidth and therefore optical noise. Lastly, Heisenberg limited detection of thermal light is undesirable because the combination of high spectral resolution and high bandwidth, results in a low *SNR*.

In brief, the author's recommendation for specific use of this thesis is as follows. The reader is encouraged to use Figure 4.6.3 when considering a highly-transient broad-wavelength absorption measurement. If thermal light is permitted, then the equations in Chapter 4 should be used to quantify the required measurement bandwidth, the required spectral resolution, and the highest *SNR* to be expected.

The conclusions above are from experimental and theoretical work by the author and are intended to serve as general design guide. In addition to these conclusions, the material in the appendix is suggested reading for a comprehensive understanding of transient broad-wavelength absorption measurements.

References

[1] Sanders,S. T., Baldwin,J. A., Jenkins,T. P., Baer,D. S., and Hanson,R. K., 2000, "Diode-Laser Sensor for Monitoring Multiple Combustion Parameters in Pulse Detonation Engines," Proceedings of the Combustion Institute**, 28**, pp. 587-594.

[2] Kranendonk,L. A., Walewski,J. W., Kim,T., and Sanders,S. T., 2005, "Wavelength-Agile Sensor Applied for HCCI Engine Measurements," Proc. Comb. Inst.**, 30**, pp. 1619-1627.

[3] Planck,Max, 1913*, The Theory of Heat Radiation*, Blakiston, Philadelphia, pp.225.

[4] Dereniak,E. L., and Boreman,G. D., 1996*, Infrared Detectors and Systems*, Wiley, New York, pp.561.

[5] Dereniak,E. L., and Crowe,D. G., 1984*, Optical Radiation Detectors*, John Wiley \& Sons.

[6] Atkins,P. W., 2001*, Physical Chemistry*, Oxford University Press, Italy, pp.997.

[7] Papoulis,Athanasios, and Pillai,S. Unnikrishna, 2002*, Probability, Random Variables, and Stochastic Processes*, McGraw-Hill, Boston, pp.852.

[8] Grimbleby,J. B., 1979, "The Ideal Averaging Filter: Its Applications and Realizations," Radio and Electronic Engineer**, 49**(10), pp. 530-4.

[9] Incropera,Frank P., and DeWitt,David P., 1990*, Introduction to Heat Transfer*, John Wiley & Sons, United States of America, pp.824.

[10] Kuhn,Thomas S., 1987*, Black-Body Theory and the Quantum Discontinuity, 1894-1912*, University of Chicago Press, Chicago, pp.378.

[11] Walewski,J. W., Filipa,J. A., and Sanders,S. T., 2006, "Optical Beating of Polychromatic Light and its Impact Ontime-Resolved Spectroscopy. Part I: Theory," Appl. Spectrosc.(In preperation.).

[12] Goodman,J. W., 1985*, Statistical Optics*, John Wiley & Sons, NY.

[13] Kraetschmer,Thilo, and Caswell,Andrew W., personal communication, 2006.

[14] Rothman,L. S., Jacquemart,D., and Barbe,A., et al, 2005, "The HITRAN 2004 Molecular Spectroscopic Database," J. Quant. Spectrosc. Radiat. Transfer**, 96**(2 SPEC ISS), pp. 139-204.

[15] Svozil,K., Calude,C. S., and Stay,M. A., 2005, "From Heisenberg to Godel Via Chaitin," International Journal of Theoretical Physics**, 44**(7), pp. 1053-65.

[16] Silfvast,W. T., 1996*, Laser Fundamentals*, Cambridge University Press, New York, NY 10011-4211, USA.

Appendix I External Cavity Diode Laser (ECDL) Experiment: *Investigation of Multi-species (H2O2 and H2O) Sensing and Thermometry in an HCCI Engine by Wavelength-Agile Absorption Spectroscopy*

Christopher L. Hagen and Scott T. Sanders

I.1 Abstract

Absorption spectra spanning 1410-1490 nm, with a spectral resolution of ~0.3 nm, were recorded in a piston engine operating in homogeneous charge compression ignition engine (HCCI) mode. Spectra were recorded every 126 μs using a wavelength-agile laser, corresponding to 0.45 CAD at the 600 rpm condition tested. The dominant absorber is H_2O vapor, but a weaker interfering absorption attributed to H_2O_2 vapor was also observed. H_2O_2 mole fraction, H_2O mole fraction, and gas temperature histories were estimated from the measured spectra. Estimated H_2O_2 mole fractions are compared to mole fractions simulated using Chemkin; the agreement is within a factor of two. This effort represents the first investigation of H_2O_2 in a combustion environment; the simultaneous measurement of multiple species in an engine by a single laser is also novel.

I.2 Introduction

HCCI engines are being developed as a next generation power plant for the automobile industry. These engines offer increased efficiencies and lower pollution potential when compared to spark ignited engines due to their omission of intake throttling and low temperature combustion.[1] Currently, however, HCCI engines are hindered by the fact that ignition is dependant on chemical kinetics and can be difficult to control relative to either spark-ignited or diesel engines. Here we present a nonintrusive combustion sensor which investigates three gas properties which are integral to the understanding of the HCCI ignition process: the concentrations of vapor phase hydrogen peroxide (H_2O_2) and vapor phase water (H_2O), and gas temperature. The combined measurement of H_2O and temperature in HCCI combustion is not novel (see, e.g., Kranendonk et al)[2]; however, the inclusion of H_2O_2 mole fraction in the same measurement represents a significant extension to the current state of the art. As described by Tanaka, the creation and destruction of H_2O_2 is a critical step to HCCI combustion because H_2O_2 molecules decompose to hydroxyl radicals (OH), feeding a chain-branching reaction leading to complete oxidation.[3, 4]

The method presented here involves investigating H_2O_2 in the near-infrared region (vibrational band centered near 1420 nm); to our best knowledge, this approach was first demonstrated in 1998.[5] For our work, we employed a rapidly-tunable (wavelength-agile) laser centered in the near-infrared (~1450 nm) to scan absorption spectra of both H_2O and H_2O_2. The individual identification of these gases is complicated by the

coincident spectra in the wavelength range probed. Rotational features of H_2O are resolved by our sensor; however, those of H_2O_2 blend together at combustion conditions to form a single, broad absorption feature (also called "diffuse" or "blended" in the literature but here referred to as "broadband"). Because of spectral overlap, the data post-processing involved deconvolution of the H_2O_2 and H_2O absorption features. This is an important extension of the work done by Kranendonk et al,[2] and requires careful consideration regarding the baseline integrity of the absorbance measurements.

This paper, which details our approach, proceeds as follows: we discuss the preliminary work to show feasibility of near-infrared combustion measurements of H_2O_2. Next the experimental apparatus and method are presented, followed by the experimental results compared with a numerical simulation. Finally, a discussion section projects our path forward.

I.3 Preliminary investigation

I.3.1 Vapor phase hydrogen peroxide (H_2O_2)

It was apparent from the literature that investigating H_2O_2 was both relevant for the general understanding of HCCI combustion and accessible at wavelengths normally used for the investigation of the $\nu_1 + \nu_3$ band of H_2O (~1300 to 1500 nm). H_2O_2 is asymmetric and has a strong affinity for decomposition to H_2O and O_2; the reaction rate for this process is heavily dependant on temperature (the rate increases by a factor of ~2.2 for

each 10° C near room temperature). A large body of literature on aqueous H_2O_2 exists; however, only limited information was found on H_2O_2, including the measured band ($\nu_1 + \nu_5$ combination band,[6] centered at ~1420 nm), the rotational constant ($B_{[0]} = 0.82$ [cm^{-1}] for H_2O_2 in its ground state[7]) and absorption coefficient.[5] Thus, we began our study by first measuring H_2O_2 absorption in a controlled environment (low pressure, long path-length cell) and second by simulating H_2O_2 and H_2O absorption spectra in the mid-infrared. The remainder of this section describes the details of this initial feasibility analysis.

I.3.2 Controlled experiment

Measurement of H_2O_2 was done in a low pressure (<1.3 kPa), long (8.9 m) cell which is double-passed to obtain 17.8 m path length at a temperature of 296 K. The low pressure was chosen to provide narrow (primarily Doppler-broadened) absorption features, which eases the identification of H_2O_2 and H_2O rotational lines. Also, the low pressure slows the decomposition of H_2O_2, allowing more time for measurements. The long path length was chosen to obtain a high absorbance. A wavelength-tunable (1380 to 1476 nm) laser (New Focus 6327) with a linewidth <5 MHz was scanned at 27 nm/s, and the transmitted intensity was detected by an amplified InGaAs photodiode (Thorlabs PDA400). Data were acquired at 100 kHz and logged by a PC-based National Instruments data acquisition system. The results of the experiment are shown in Figure I.3.1.

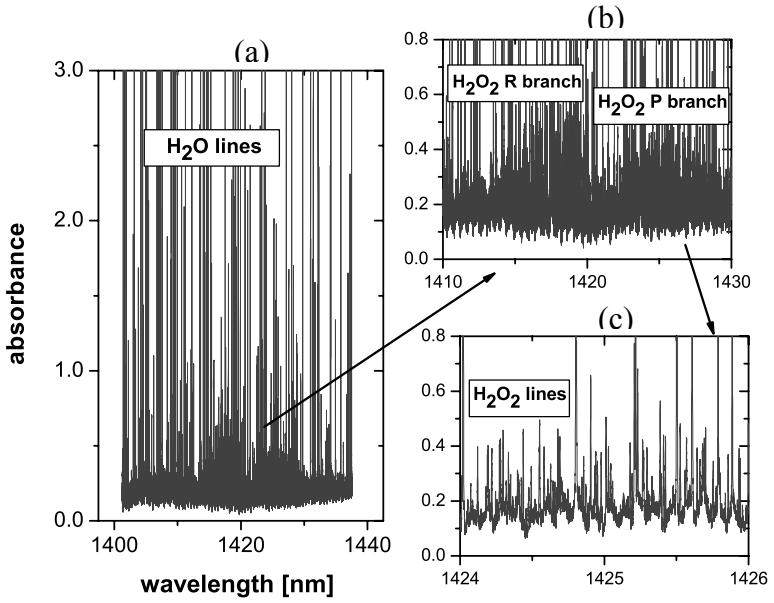

Figure I.3.1a. **H_2O_2 and H_2O absorbance measurements at 0.8 kPa, 296 K and a path length of ~17.8 m (relative concentrations unknown).** b. **Zoom of expected H_2O_2 absorption location.** c. **Zoom showing individual H_2O_2 lines in the midst of taller H_2O lines. The minimum detectable absorbance of this measurement was ~0.04** ***[unit1].***

As can be seen in Figure I.3.1a, H_2O absorption in the cell was strong and nearly obscures H_2O_2. However, Figure I.3.1b is a zoom highlighting the expected H_2O_2 region where H_2O_2 R and P branches and the associated rotational lines can be easily distinguished. Due to the observed congestion of the H_2O_2 lines, the low-pressure cell results suggest that H_2O_2 at engine conditions will constitute a broadband absorber. Thus, in the engine, distinguishing H_2O and H_2O_2 will be more difficult than in Figure I.3.1. However, it is clear from Figure I.3.1 that the opportunity to measure H_2O_2 under

engine conditions does exist, provided a scheme for deconvolving H_2O_2 and H_2O can be implemented.

I.3.3 Simulated H_2O_2 and H_2O spectra

An expectation corroborated by Figure I.3.1 is that H_2O may generally be a stronger absorber than H_2O_2, and thus the former may obscure the latter in combustion environments. To assess this concern, the spectroscopic database HITRAN[8] was incorporated to estimate the relative absorption strengths of H_2O_2 and H_2O as well as the temperature effects on H_2O_2 spectra. As previously mentioned, spectral information on H_2O_2 in the near-infrared was not readily available, so *simulations at wavelengths other than the experimental wavelengths were investigated for qualitative purposes only*. In HITRAN, the H_2O_2 data nearest our wavelength of interest was a collection of lines spanning 6.6 to 13 μm. We chose a fundamental vibrational band in the 7.4 to 8.4 μm range from HITRAN and simulated absorption strengths at two temperatures (296 and 900 K). These results were compared with a fundamental H_2O vibrational band (2.4 to 3.0 μm), at the same temperatures. The results of the simulation are shown in Figure I.3.2.

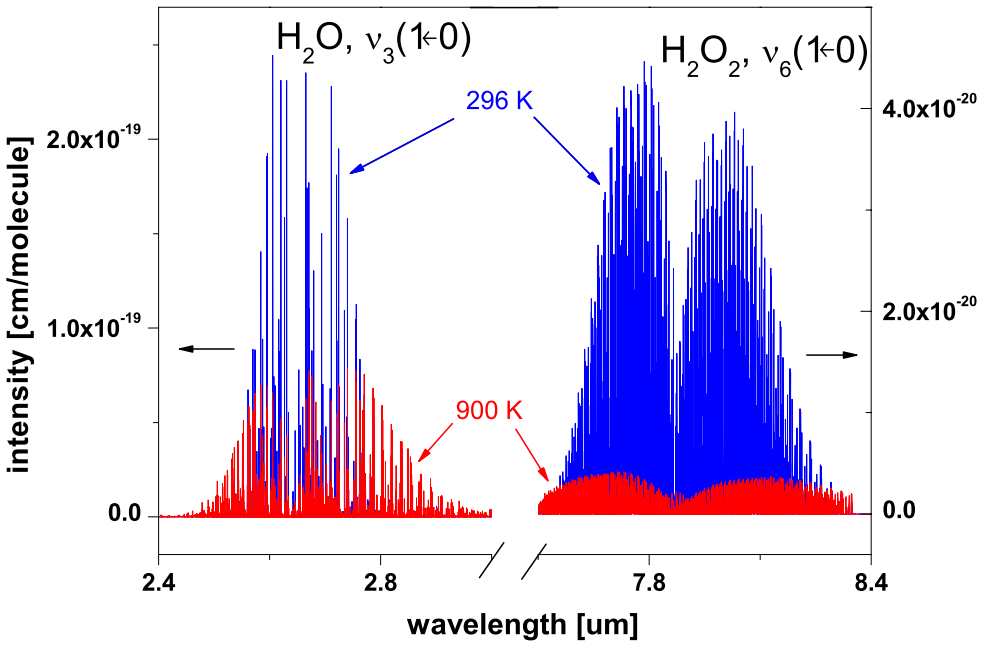

Figure I.3.2 Absorption line intensity simulations (HITRAN) of H_2O_2 and H_2O. Vibrational band locations were chosen based on HITRAN's H_2O_2 which was spectrally close to the region of interest and strong. Note the difference in both line densities and the ratio of line heights for the two species.

Three key pieces of information can be obtained from Figure I.3.2. First, the relative line density of H_2O_2 is ~ 5 times that of H_2O. In fact, the H_2O_2 features are sufficiently congested that one would expect broadband absorption under typical engine conditions. Second, individual H_2O_2 absorption line heights decrease with temperature more dramatically than the H_2O line heights, as is typical for larger molecules. Third, the rotational envelopes for both molecules spread (spectrally) from band center with increasing temperature at similar rates.

Specifically, Figure I.3.2 reveals that the H_2O_2 absorption was reduced by a factor of ~10 from 296 K to 900 K, whereas H_2O absorption was reduced by a factor of only ~3 over the same temperature range. This might lead one to expect that, relative to H_2O, H_2O_2 will be increasingly more difficult to measure as temperature increases; however, this conclusion is only valid for spectroscopy of rotationally resolved features. Under the broadband absorption condition for H_2O_2 in engines, the integrated absorbance area of the entire (blended) H_2O_2 band is a constant for a given H_2O_2 number density, and thus the discouraging 10:3 ratio mentioned above is tempered. In effect, when the total integrated absorbance area is considered, the decreasing line heights relative to H_2O are exactly compensated by the increased line density. Furthermore, because the spectral widths of the entire rotational envelopes for both H_2O_2 and H_2O increase in a similar fashion as temperature increases (there is no exaggerated spectral broadening of the rotational envelope for H_2O_2 relative to H_2O), high temperatures alone should not enhance obscuration of H_2O_2 by H_2O. Our conclusion from Figure I.3.2 was that H_2O_2 measurements might indeed be possible in an engine environment, particularly in an environment where the concentrations of H_2O_2 and H_2O are similar.

I.4 Materials and methods

I.4.1 The Laser

Since the laser used for the low pressure test scanned relatively slow (~3.5 sec/scan), a faster scanning laser was chosen for the engine experiment. The selected laser was an external cavity diode (ECDL) laser configured for modeless operation which was a modified version of the laser developed by Kranendonk et al[9] . In short, the cavity length of this ECDL changes as part of the wavelength tuning approach (vibrating mirror

and stationary grating) and therefore avoids issues such as mode hopping. The ECDL, shown schematically in Figure I.4.1, has an instantaneous spectral width of ~0.3 nm. In our case the laser was scanned from 1410 to 1490 nm in 63 μs and back to 1410 nm in the next 63 μs, corresponding to a repetition rate of 8 kHz (every 0.45 crank angle degrees (CAD) for an engine at 600 rpm). Between these scans the mirror momentarily directs the light off of the grating. This feature allowed a short "laser off" period during each laser scan which was later used to correct detected signals for thermal emission.

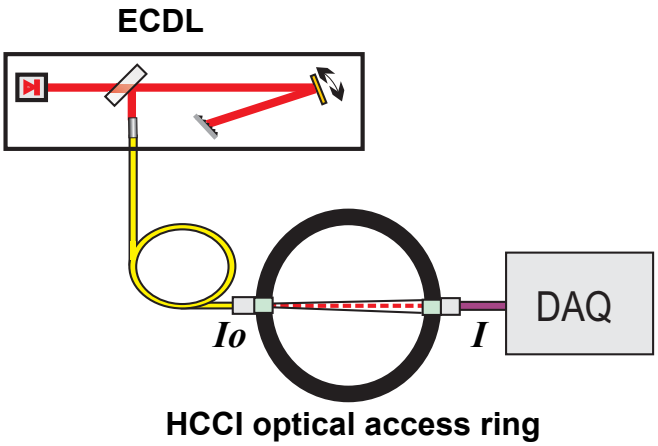

Figure I.4.1 Schematic of experimental arrangement. The modeless external cavity diode laser (ECDL) sends light via a single mode fiber to a columnation package (Io). From the columnation package the light traverses the HCCI optical access ring and is collected by a photodiode (I).

The light from the ECDL is coupled into a single mode fiber connected to a collimation package in the optical access ring of the engine. The lenses used to collimate the light

through the engine were chosen based on Kranendonk et al[10] in an effort to mitigate beemstearing.

I.4.2 The engine

The single-cylinder optical engine investigated here is the same as in our previous work.[11] The engine has a Bowditch-style piston that allows lubricant-free operation of the combustion chamber. A spacer ring fitted with two diametrically opposed sapphire windows (12 mm diameter, 9-mrad wedge) allows optical access to the combustion chamber. The latter houses a 9.24-cm diameter piston which makes a 7.63 cm stroke resulting in a compression ratio of 9.64:1. The optical path through the cylinder is 9.5 cm long.

The input air to the cylinder was delivered through a critical-orifice assembly set at a flow of 2.1 g/cycle and atmospheric intake pressure. The intake air stream was electrically preheated at 363 K and the temperature of intake and exhaust were monitored with type-K thermocouples. The in-cylinder pressure was monitored with a piezoelectric transducer (Kistler 7063) in combination with a charge amplifier (Kistler 5004). Transducer, cable and charge amplifier were calibrated as a system with a dead-weight tester. The coolant to the engine was preheated and maintained at 343 K. The n-heptane fuel was injected into the intake air 1 m upstream from the intake valve. By so doing a high level of uniformity of the fuel-air mixture was achieved.[11] In the experiments reported here the engine was operated at 600 rpm and an equivalence ratio of $\Phi = 0.16$.

I.4.3 Data acquisition

After passing through the engine cylinder, the transmitted light is collected by an aspheric lens and focused onto a 10 MHz InGaAs photodiode (Thorlabs PDA400). The signal from the photodiode was digitized by a 4 GHz digital oscilloscope (Tektronics TDS7404).

As previously mentioned, our mole fraction measurements of H_2O_2 relied on detecting broadband absorption, which means that the measurements must be free of any baseline artifacts resulting from the division of collected light (*I*) by incident light (*Io*). This constraint has generally not been relevant in previous wavelength-agile absorption spectroscopy work[2] where H_2O absorption spectra were collected, smoothed, and *differentiated to remove the baseline* and fit only the absorption peaks.

In the work presented here, we incorporate a three-pronged baseline-preserving approach which involves using a single detector to eliminate detector difference errors, collecting data in the gas-exchange stroke as well as the compression stroke, and engine cycle averaging. Data were collected at a selected CAD during the firing engine stroke (*I*) and exactly 360 CAD later during the ensuing gas exchange stroke (*Io*, in the absence of H_2O_2 and high temperature water). Utilizing a single detector for both *I* and *Io* eliminated possible electrical ambiguities which can be seen when using separate *I* and *Io* detectors. Also, by collecting *I* and *Io* within a 100 ms time window, baseline artifacts from temporal laser drift are minimized. Finally, data was collected over 150 engine cycles to be averaged in post-processing to reduce baseline noise.

I.4.4 Post-processing

The per-engine-cycle I and I_0 signals collected were averaged using codes written in LabVIEW. The averaged spectra, which were offset during combustion by thermal emissions, were corrected by treating the "laser off" signal levels as DC offsets. The magnitudes of the maximum emission (occurring ~ at top dead center, TDC) and the transmitted light were approximately equal. The offsets due to emission were subtracted from their respective I spectra. Examples of resulting spectra are shown at their respective CAD positions on the cylinder-pressure plot in Figure I.4.2. The two-stage heat release characteristic for HCCI combustion (referred to as first- and second- stage combustion, respectively) can also be seen in Figure I.4.2.

Prior to first-stage combustion, the absence of H_2O_2 is clear, with weak H_2O absorption visible. Between first- and second-stage combustion, the presence of H_2O_2 is also clear as a broad feature upon which the narrower H_2O features ride. Following second-stage combustion, there is negligible H_2O_2 present; although remnants of the broad H_2O_2 feature may appear to be present in Figure I.4.2 (top right inset), this broad sloping trend is actually due entirely to H_2O as verified by our spectral fitting scheme discussed below.

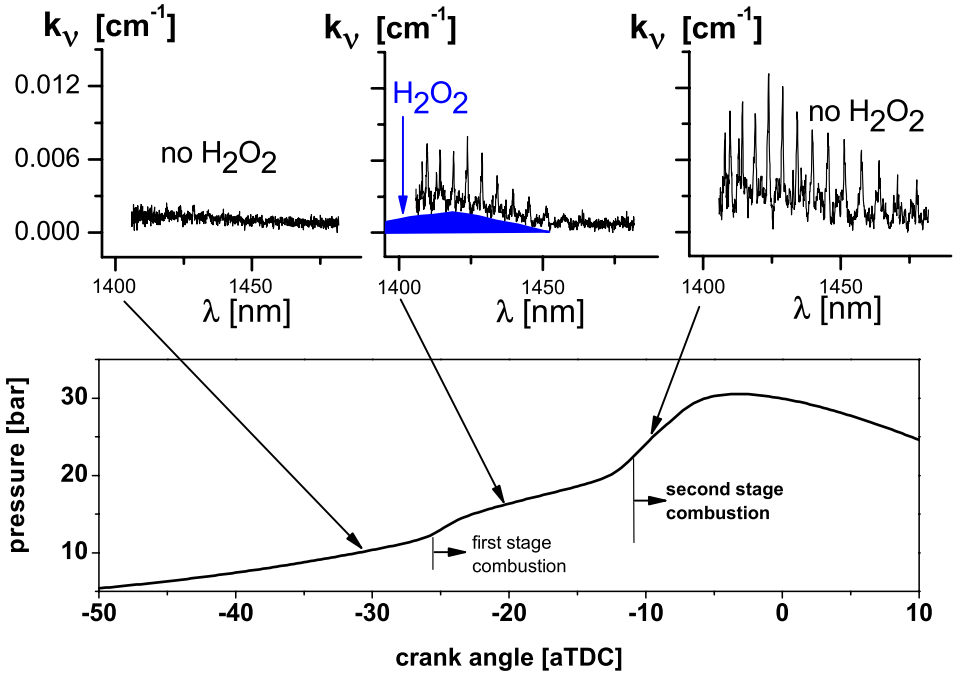

Figure I.4.2 Collected absorption spectra during pre-first stage, intermediate stage and second stage HCCI combustion respectively, where kv is absorption coefficient [cm-1] and λ is wavelength [nm].

Spectra were processed to determine water mole fraction and temperature, as reported elsewhere, [2] by the use of the Beer-Lambert Law[12] shown in Equation 1.

Equation 1 $$\alpha_v = -ln(I/Io) = k_v \cdot L$$

Where $\boldsymbol{\alpha_v}$ is the absorbance *[unit 1]*, *I* is the collected light signal *[V]*, *Io* is the incident light signal *[V]*, k_v is the spectral absorption coefficient *[cm^{-1}]*, and *L* is the path length *[cm]*.

Next, to determine the mole fraction of H_2O_2 (χ_{H2O2}), the difference between the experimental spectra and the inferred H_2O ($\nu_1 + \nu_3$) HITRAN simulation spectra from the previous step was calculated. The residual spectra containing primarily the H_2O_2 broadband absorption was fit with a broad Gaussian shape, centered at 1420 nm and with a full width at half maximum of 40 nm, as determined in the fitting process. A fit for one -12 CAD aTDC is shown in Figure I.4.3.

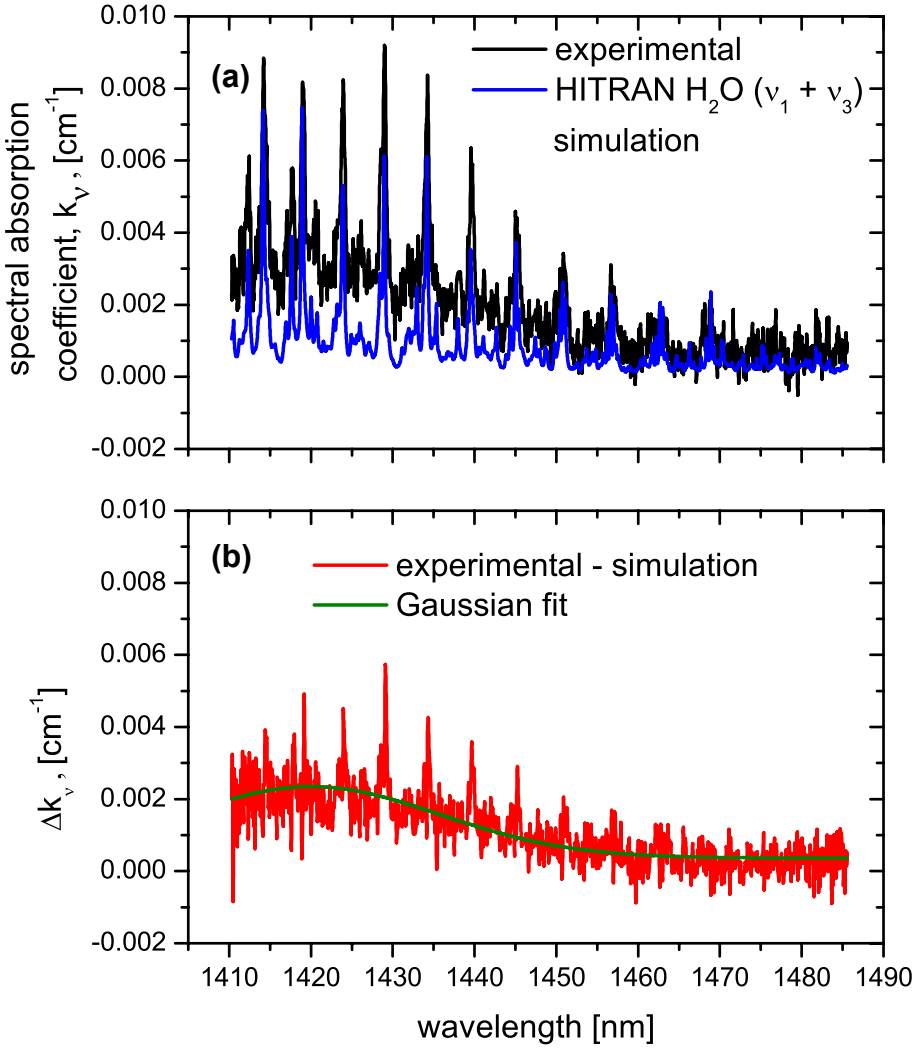

Figure I.4.3 a. Example experimental and simulated spectra for the process used to determine H2O2 mole fraction at -12 CAD aTDC for a 150 cycle average. b. Fit of a Gaussian shape to the residual of the experimental and simulated H2O spectra, the area of the Gaussian is the integrated absorbance for peroxide, AH2O2 [cm-1]. The minimum detectable absorbance of this measurement, , kv noise·L, was ~0.004 [unit 1].

The wavelength range of ~1460 to ~1485 nm are essentially nonabsorbing wavelengths for water and peroxide in the precombustion and intermediate stage combustion portions

of the experiment due to lower temperatures, as seen in Figure I.4.3. This ~25 nm range was flat, without any data manipulation, over the portion of the engine cycle where peroxide mole fraction was fit, indicating reliable baseline integrity and the absence of beamsteering with a chromatic dependence.

Because there was no apparent chromatic-beamsteering, the entire broadband feature fit by the Gaussian in Figure I.4.3 was attributed to H_2O_2. It is possible that other broadband absorbers (molecules roughly as large as H_2O_2 or larger) could invalidate this assumption; however, to absorb in this range most likely requires that they contain an -OH group, and all such molecules are expected to be present in negligible concentration based on our Chemkin analysis (see below). The integrated absorbance, A_{H2O2} $[cm^{-1}]$, was extrapolated from each Gaussian fit because the full vibrational band was not probed. The relationship between integrated absorbance and spectral absorption coefficient, k_ν $[cm^{-1}]$, is represented mathematically in Equation 2.

Equation 2

$$A_{H2O2} = \int_{-\infty}^{+\infty} k_\nu d\nu$$

A band strength $S(T_{Ref})_{H2O2}$ of 12 ± 2 $[bar^{-1}cm^{-2}]$ of H_2O_2 in the selected wavelength range was estimated from Adams,[5] where T_{ref} was 296 K. We assumed that the band strength is independent of temperature; however, it was necessary to include a T_{ref}/T term, shown in Equation 3, in our calculation for to account for reduced number density at fixed pressure associated with the ideal gas law. The Band strength is independent of temperature if the fractional population of the vibrational ground state and the excited vibrational states are each independent of temperature, which depends on the energy

difference between ground state and excited states. If the difference between is rather large, the higher lying levels remain only weakly populated for the temperatures considered in this work. We corroborated the previous statement by calculating the fractional population of the vibrational levels with equations and vibrational energies reported elsewhere.[7, 13] The combined population of the ν_1 and ν_5 state were found to be 5% or lower for temperatures below 1000 K. Therefore, the absorption would change not more than 5% due to thermally induced population transfer. However, the H_2O_2 molecule sustains other modes of vibration, which are not directly involved in the probed transition. The transfer in such "hidden" states has a potentially stronger impact on the absorption strength. One of these state, ν_4, has a ten times smaller vibrational energy than the both ν_1 and ν_5 level. Higher lying vibrational levels in this band populate already at rather low temperatures, and the population of the vibrational ground state decreases by ~ 25% when increasing the gas temperature from 300 to 1000 K. This thermally induced population transfer will certainly affect the band strength since it shifts ground state molecules into potentially non-absorbing higher vibrational states, and we are assessing the minimum and maximum influence as follows. In the case that the $\nu_1 + \nu_5$ transition also can occur from higher lying ν_4 levels, and that these transitions exhibit a noticeable band strength, a transfer of population to higher lying ν_4 states would not change the absorption strength of the probed transition. The strength would only decrease by about 5% due to the above discussed transfer of population to the ν_1 and ν_5 levels. However, if the possibility for such transitions is very low, the higher lying ν_4 levels will not absorb the laser light, and the band strength decreases by 25% over the above temperature range due to the population transfer from the ground state to the higher lying non-absorbing ν_4

levels. Additionally there would be a transfer of 5% to the ν_1 and ν_5 levels, so that the total change in band strength would add up to 30%. In conclusion, we estimate the error in band strength, attributed to the temperature independence assumption, to be between a minimum of 5% and a maximum of 30%.

Next, Equation 3, adapted from Rao,[12] was applied; using pressure data from the transducer, temperature inferred from the water fit, and a known path length; to determine mole fraction of H_2O_2:

Equation 3

$$\chi_{H2O2} = \frac{A_{H2O2}}{S(T_{\mathrm{Re}f})_{H2O2} \cdot \frac{T_{\mathrm{Re}f}}{T} \cdot P \cdot L}$$

Where χ_{H2O2} is the mole fraction of peroxide *[unit 1],* A_{H2O2} is integrated absorbance for peroxide *[cm^{-1}]*, $S(T_{ref})_{H2O2}$ is band strength *[$bar^{-1}cm^{-2}$]*, T_{ref} is the reference temperature for the band strength *[K]*, *T* is temperature of the gaseous experiment *[K]*, *P* is the total absolute pressure of the experimental gasses *[bar]*, and *L* is the path length of the experiment *[cm]*.

A single-zone adiabatic numerical engine simulation was run in Chemkin 4.0 under the experimental conditions using the Chalmers University 40 species n-heptane mechanism.[14] The measured and numerical simulation data are compared in the following section.

I.5 Results

The experimental and simulation data are shown in Figure I.5.1.

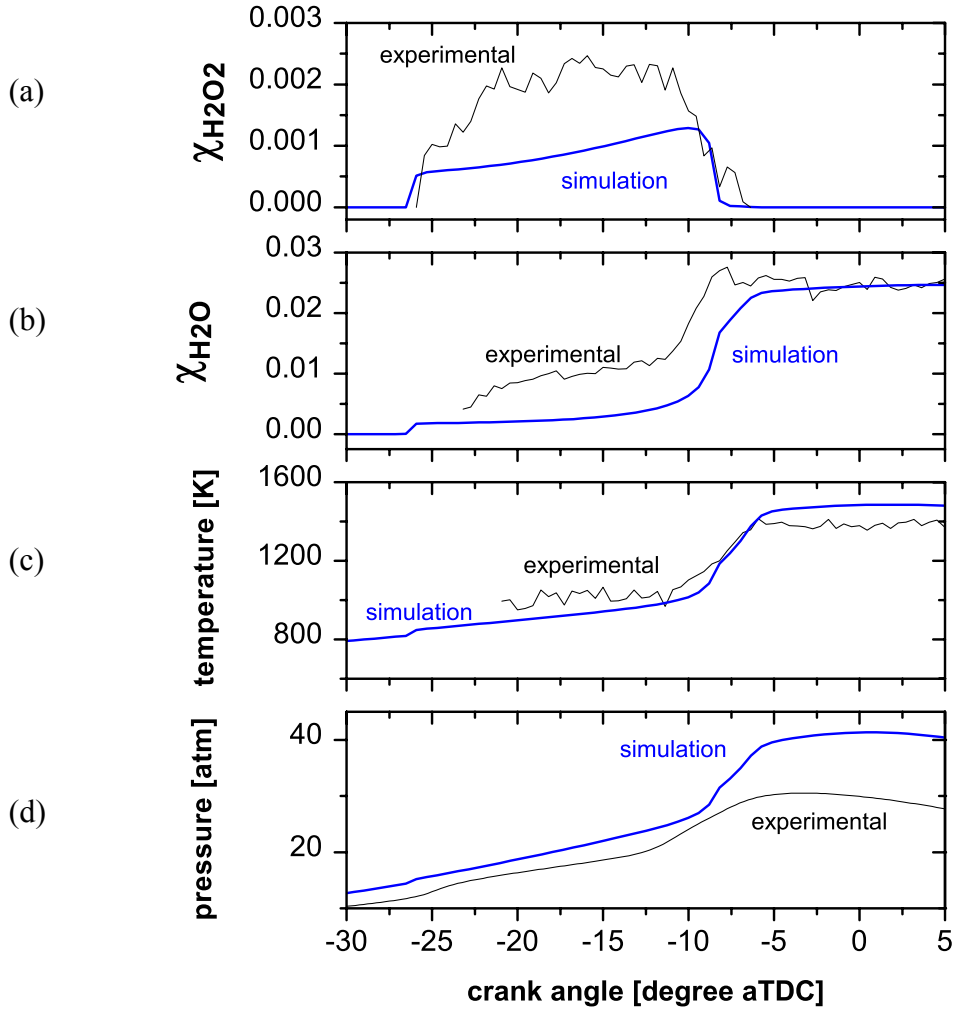

Figure I.5.1 Experimental (150 cycle average) and Chemkin model simulation results as a function of CAD for engine operating in HCCI mode on n-heptane with rc = 9.64, Tinlet = 363 K, Pinlet = 1 bar, Φ = 0.16. Curves are truncated by inspection, for example where too little H2O is present to make reliable temperature measurements.

The experimental data in Figure I.5.1 represents an average of 150 engine cycles. Figure I.5.1a shows the experimental and simulated H_2O_2 mole fraction data. The experimental values are found to be systematically larger than what the simulation predicts. This discrepancy may be due to factors such as: the uncertainty in the band strength estimate, the band strength temperature independence assumption, or under prediction by the Chemkin model. In Figure I.5.1b, it is seen that the experimental H_2O mole fraction is slightly higher during intermediate combustion as observed previously in Kranendonk et al;[2] improved chemical mechanisms may be required to reduce this discrepancy. Figure I.5.1c shows that the simulated model reaches a peak temperature above the experimental data. Again, since the model is ideal and adiabatic, this result was expected. In Figure I.5.1d a large discrepancy in the pressure data was recorded. The engine used here is known to have significant blowby at elevated pressures resulting in dramatically reduced peak pressures. However, in spite of these less than ideal factors, temperature and water mole fraction determined by this technique can be accurate within ~±2%[2][15] under refined conditions. The hydrogen peroxide mole fraction measurement accuracy, on the other hand, was predicted to be no better than 34% primarily due to the band strength uncertainty.

I.6 Discussion

In this paper we have shown a first-ever, nonintrusive, in-cylinder, investigation of H_2O_2 mole fraction. Furthermore, we have demonstrated the ability to monitor multiple species

as well as gas temperature using a single wavelength-agile laser in an engine environment. Finally, we have demonstrated that broadband and rotational-featured spectra, even if they overlap, can be discerned in a practical environment. It is noteworthy that if H_2O_2 was the only absorber present in our wavelength range, we could use an absorption spectrometer with low spectral resolution (e.g., based on a grating spectrometer at the engine output) to monitor its concentration. However, with H_2O present, as is generally unavoidable, the low-resolution spectrometer would not be able to discern H_2O and H_2O_2 as we have done here.

As mentioned, measurements of H_2O_2 are of significant importance for understanding the chemical kinetics associated with HCCI combustion. Looking to the future, we hope to improve our multi-species sensor by primarily focusing on improvements in the H_2O_2 measurement. For example, we plan on tailoring the spectroscopic portion of the experiment for this measurement by using a faster scanning laser with a broader spectral range centered near 1420 nm, capturing the full vibrational band of H_2O_2 and thus improving the precision of the H_2O_2 measurements. Additionally, experiments are planned to better estimate the band strength of H_2O_2 in this spectral region, thus improving the accuracy of the H_2O_2 measurements. As a final step, we hope to measure H_2O_2 over a range of engine operating conditions (fueling, diluents, and RPM), ultimately leading to a more complete understanding of low-temperature combustion chemistry.

Acknowledgements

The authors thank Ms. Laura Kranendonk, Mr. Andrew Caswell and Dr. Joachim Walewski for technical assistance. This material is based on work supported by the National Science Foundation under grant 0238633.

References

[1] Stanglmaier,R. H., and Roberts,C. E., , "Homogenous Charge Compression Ignition (HCCI): Benefits, Compromises, and Future Applications," SAE Paper 1999-01-3682.

[2] Kranendonk,L. A., Walewski,J. W., Kim,T., and Sanders,S. T., 2005, "Wavelength-Agile Sensor Applied for HCCI Engine Measurements," Proc. Comb. Inst.**, 30**, pp. 1619-1627.

[3] Tanaka,Shigeyuki, Ayala,Ferran, and Keck,James C., 2003, "A Reduced Chemical Kinetic Model for HCCI Combustion of Primary Reference Fuels in a Rapid Compression Machine," Combust.Flame**, 133**(4), pp. 467-481.

[4] Glassman,Irvin, 1996*, Combustion*, Academic Press, Inc., San Diego, pp.631.

[5] Adams,D., Brown,G. P., Fritz,C., and Todd,T. R., 1998, "Calibration of a Near-Infrared (NIR) H202Vapor Monitor," Pharmaceutical Engineering**, 18**(3), pp. 1.

[6] Giguere,Paul A., 1950, "The Infra-Red Spectrum of Hydrogen Peroxide," J. Chem. Phys.**, 18**(1), pp. 88.

[7] Herzberg,Gerhard, 1945*, Molecular Spectra and Molecular Structure*, Krieger, Malabar, FL, pp.636.

[8] Rothman,L. S., Jacquemart,D., and Barbe,A., et al, 2005, "The HITRAN 2004 Molecular Spectroscopic Database," J. Quant. Spectrosc. Radiat. Transfer**, 96**(2 SPEC ISS), pp. 139-204.

[9] Kranendonk,L. A., Bartula,R. J., and Sanders,S. T., 2005, "Modeless Operation of a Wavelength-Agile Laser by High-Speed Cavity Length Changes," Opt. Express**,** **13**(5), pp. 1498-1507.

[10] Kranendonk,L. A., and Sanders,S. T., 2005, "Optical Design in Beam Steering Environments with Emphasis on Laser Transmission Measurements," Appl. Opt.**,** **44**(31), pp. 6762-6772.

[11] Sanders,S. T., Kim,T., and Ghandhi,J. B., 2003, "Gas Temperature Measurements during Ignition in an HCCI Engine," SAE 2003-01-0744.

[12] RAO,K. N., 1976, "Molecular Spectroscopy: Modern Research," **, II**(12/01/2005), pp. 279.

[13] Linne,Mark A., 2002*, Spectroscopic Measurement : An Introduction to the Fundamentals*, Academic Press, Amsterdam ; Boston, pp.414.

[14] Nordin,N., 1998" ", Chalmers University of Technology, Licenciate of Engineering.

[15] Kranendonk,L. A., Huber,R., Fujimoto,J. G., and Sanders,S. T., 2007, "Wavelength-Agile H_2O Absorption Spectrometer for Thermometry of General Combustion Gases," Proc. Comb. Inst.**, 31**

Appendix II Thermal Emitter (TE) Experiment: *Toward hyperspectral sensing in practical devices: measurements of fuel, H2O, and gas temperature in a metal HCCI engine*

Christopher L. Hagen and Scott T. Sanders

II.1 Abstract

Absorption spectra of H_2O ($\nu_2 + \nu_3$ band, R branch) and C_8H_{18} (C-H stretch overtone, entire band) were measured in a piston engine using a lamp and spectrometer. Spectra were taken at a rate of 900 spectra second^{-1} over the 1600 nm – 1850 nm range with a resolution of 0.75 nm (3.0 cm^{-1}). A grating spectrometer based on an extended indium gallium arsenide (x-InGaAs) linear array camera was used. The engine is an isooctane-fueled homogeneous charge compression ignition (HCCI) engine operating at 1000 RPM. Spectra were post processed for in-cylinder temperature, H_2O density, and fuel density. Fuel spectra measured near autoignition conditions differ slightly from room-temperature spectra as expected. Using 1000-cycle averaging in the engine, we achieved a broadband minimum detectable absorbance of less than 1%.

II.2 Introduction

Our vision is to develop instrumentation for monitoring absorption spectra in practical devices. The ideal instruments would have broad wavelength coverage (spanning the ultraviolet ~ 0.2 μm to the infrared ~ 20 μm), high-resolution (~ 0.1 cm^{-1}), rapid rates (~ 10 kHz, or 1 spectrum every 100 μs), and high signal-to-noise ratio (minimum detectable absorbance, MDA ~ 0.1%). These specifications, although extreme, do not violate any fundamental laws. Such instruments would be valuable because they would allow quantitative measurements of many species, simultaneously, in transient environments such as engines. For instance, with sufficient performance, it may be possible to monitor fuel decomposition chemistry in engines by tracking the concentrations of small hydrocarbons. Results, in turn, can be used to enhance kinetic models by providing empirical data for refining chemical mechanisms.

Designing such instrumentation is a challenging proposition not likely to be realized soon. However, recent measurements show progress; example systems with promising specifications include a Fourier domain mode locked system (1330-1380 nm, 0.5 cm^{-1}, 200 kHz, 8% MDA)[1], a lamp/spectrometer arrangement (270-330 nm, 180 cm^{-1}, 2 kHz, 70% MDA) [2], and a diode-laser-based sum-frequency generation system (313.52-313.53 nm, 0.001 cm^{-1}, 20 kHz, 12% MDA)[3]. In this paper, we describe a system covering the 1600-1850 nm range, with 3 cm^{-1} resolution, 1 kHz spectral rate, and a single-scan MDA of 20%. Although this system remains well short of the ideal, it is clear how to extend each parameter closer to the desired value (for example, an echelle format spectrometer

can provide broader wavelength coverage at high resolution). Furthermore, even in its current form, the system represents a versatile sensing tool which is based on user-friendly commercial components, allowing easy adaptation to numerous sensing problems.

We are currently studying Homogeneous charge compression ignition (HCCI) engines because they are both important to the future of transportation and they are compatible with absorption measurement techniques. HCCI engines have shown promise as a next generation automotive power plant because they offer reduced emissions and increased efficiency as compared to conventional spark ignited and diesel engines[4]. However, the initiation of combustion in an HCCI engine is dependent almost exclusively on chemical kinetics, and at this time, no analog to spark or injection control exists. Therefore, empirical studies are being performed to understand HCCI ignition chemistry. Absorption spectroscopy, an integrated line-of-sight technique, is well suited for characterizing HCCI combustion because, as the name implies, the in-cylinder charge is homogeneous and therefore an average measurement is often meaningful.

In previous work, two such absorption measurements have been performed in HCCI engines: a wavelength-swept laser technique used to monitor multiple species, and a lamp/spectrometer technique used for single species analysis. For the wavelength-swept measurement, Hagen et al[5] used a near-infrared external cavity diode laser[6] (1410-1490 nm range, 1.5 cm^{-1} resolution) to monitor H_2O and H_2O_2 concentrations from which in-cylinder temperature could also be inferred. In that measurement, the post-processing of

the measured spectra was difficult because of complete spectral overlap of H_2O_2 and H_2O spectra. In the second example, Younger[2] used an ultraviolet lamp and spectrometer (280-320 nm range, 180 cm^{-1} resolution) to measure OH concentration. However, the low spectral resolution of the data prevents reliable identification of OH when multiple absorbers are present. Furthermore, the low spectral resolution disables the ability to process the spectra for in-cylinder temperature.

The thrust of this paper is a multispecies absorption spectroscopy measurement using a lamp and spectrometer. The notable differences between the present work and the previous work are the species chosen and the sensor system resolution. Here, two species with spectrally separated absorption spectra, isooctane (C-H stretch first overtone) and H_2O ($\nu_2 + \nu_3$, R branch), were measured in the near-infrared (1600-1850 nm range). Furthermore, relative to the previous lamp/spectrometer system, the spectral resolution was improved from 180 cm^{-1} to 3 cm^{-1}. The increased resolution allowed us to measure unambiguous species concentrations and in-cylinder temperature.

II.3 Method and materials

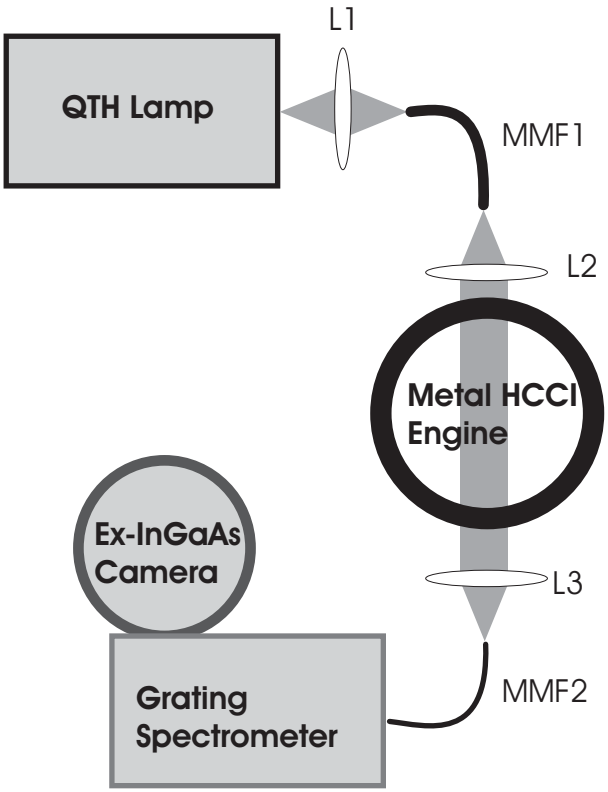

Figure II.3.1 Experimental fiber coupled engine arrangement consisting of a quartz tungsten halogen (QTH) lamp, 550µm multimode fiber (MMF1), lenses (L1, L2 and L3), a metal single-cylinder homogeneous charge compression ignition (HCCI) research engine, 62.5µm multimode fiber (MMF2), and an extended Indium Gallium Arsenide (x-InGaAs) camera coupled grating spectrometer.

The experimental arrangement, used for both the preliminary investigation and for the results to be presented, is shown in Figure II.3.1. The system consisted of three major

components; the light source, the engine, and the spectrometer. The components were coupled together by multimode optical fiber.

II.3.1 Light source and optics

This experiment required a near-infrared light source centered near 1725 nm spanning more than 200 nm. The center wavelength was chosen so that H_2O and isooctane absorption bands would both be recorded. The spectral breadth of the measurement was necessary to record greater than 60 nm of non-absorbing baseline in order to validate baseline integrity. Two broadband candidates in the desired wavelength range were a supercontinuum (SC) source and a quartz tungsten halogen (QTH) lamp.

II.3.1.1 Supercontinua

Fiber coupled SC are broadband sources which are generated by focusing a high power laser into a fiber optic cable. Spectral broadening of the pump by a number of nonlinear optical processes is possible[7]. Sources of this type([8]) ([9]), are capable of spanning 100s nm of the visible to mid-infrared with average powers greater than 5 mW. These sources are attractive because they are fiber coupled and they achieve spectral radiances [$Wm^{-2}sr^{-1}\mu m^{-1}$] at least 10^3 times that of thermal emitters[89].

For the purpose of this experiment, we built a 50 MHz repetition rate femtosecond SC using an Erbium fiber laser (IMRA A50, $\lambda_{ceneter}$= 1560 nm, 2.5 nJ $pulse^{-1}$, 300 fs pulse

duration) coupled to a single-mode photonic crystal fiber (PCF, Crystal Fibre NL-1550-NEG-1). This arrangement generated broadband light primarily by self-phase modulation (SPM) with an average output power of ~2 mW from 1600-1850 nm. Because this SC is a result of SPM, it exhibits lower noise than typical pulsed nanosecond SC ([10]). The latter can be approximated as bright, pulsed thermal emitters, which generally have high noise for the timescales of interest in engine experiments[11]. However, even the femtosecond SC that was built for the present experiment has appreciable noise, the sources of which included stimulated Brillouin scattering, stimulated Raman scattering, and fluctuations in pump energy. Noise reduction was accomplished through multi-pulse averaging. The camera, described below, was able to integrate over ~10,000 pulses and therefore reduce the apparent noise. Preliminary measurements were made with the SC source and grating spectrometer through air on a laboratory bench top, the results of which revealed the importance of polarization.

II.3.1.2 Polarization

Polarized light sources have been used successfully for engine measurements ([112]). However, since the grating spectrometer that was used in these experiments was highly sensitive to polarization, due primarily to the ruled diffraction grating installed, any change in polarization over time was problematic. The primary issue in the initial bench top experiment was the change in polarization due to changes in stress of the SMF. Light polarization is preserved for any length of a perfectly circular core fiber which has no strain. Polarization in real fibers, on the other hand, is shifted due to manufacturing

imperfections and strain[13]. Thus, any small disturbance to the SC-carrying SMF resulted in large changes in the apparent spectrum measured by the camera. Three approaches to mitigating this wandering polarization are to either select a grating which is equally efficient in both the S and the P planes, use polarization maintaining fiber, or to use randomly polarized light. It is difficult to manufacture diffraction gratings with exactly the same efficiency in the S and P planes over broad spectral ranges. However, polarization maintaining fiber (PM) and randomly polarized light are both available. The former will be discussed here and the latter will be presented in a subsequent section.

Polarization maintaining fiber is single mode fiber manufactured with internal strain which forces the two polarization planes to propagate at different velocities[14]. Measurements using PM fiber on the bench top were promising. Therefore, the engine was outfitted with (single-mode) PM fiber at both the input and output locations. Of course, SM-to-SM coupling through an engine causes intense beamsteering sensitivity. One solution that was considered was to use a very large pitch beam, which can be created by defocusing the SM pitch light and is effective in reducing beamsteering sensitivity. However, this reduction comes at the cost of reduced throughput. An SC ~50 times brighter would be needed to reach a solution in this fashion. However, we are concerned that even with such a bright SC, engine window birefringence could cause polarization-related noise.

During the experiments, specifications for an acceptable SC source were developed. When the specifications in Table II.3.1 are met, SC sources will attractive alternatives to

lamps. The SC used in these experiments fell short with respect to polarization and temporal drift, so a lamp was, in the end, superior. A SC that could meet the table 1 specifications would offer improved performance over the lamp because of the single-mode output (MMF1 shown in Figure 1 could be replaced by SMF). A SC offering the table 1 specifications, but with ~ 100 mW power would enable a superior all SM-fiber system (both MMF1 and MMF2 in Figure 1 could be replaced by SMF, eliminating all noise associated with multimode fibers). Finally, a SC offering table 1 specifications, but with ~ 1W power would enable an all-fiber system with sufficient power for single-shot measurements with MDA less than 1%.

Table II.3.1 Desired supercontinuum (SC) specifications for absorption measurements

Attribute	**Specification**
Spectral coverage	1600 - 1850 nm, spectral ripple < 6 dB
Output coupling	Single-mode fiber
Power (average)	> 2 mW
Polarization	Depolarized
Temporal drift	< 0.1% change in spectrum over 1 s
Operating mode	CW or quasi-CW (rep rate > 10 kHz, duty cycle > 10% for a quasi-thermal emitter)

II.3.1.3 QTH lamp

Because of the shortcomings of present SC identified above, a multimode fiber-coupled thermal emitter was chosen for the present measurements. This source was stable,

randomly polarized, turnkey, inexpensive, and broadband. Again, the only significant drawback, relative to a SC, is the spectral radiance. Because of the low radiance, multimode fibers were necessary for both the engine input and output. Unfortunately, multimode fibers can cause mode noise in the measured spectra. Furthermore, a tradeoff exists between the larger multimode fiber leading to the spectrometer and spectral resolution. However, the introduction of mode noise and the reduction of resolution were offset by the positive thermal emitter attributes mentioned above.

The thermal emitter used in these experiments was a 20W quartz tungsten halogen (QTH) lamp (Oriel 6319) which had a blackbody emission profile for a temperature of ~3200 K and an effective emissivity of 0.27 from 1600nm to 1850 nm. The lamp light was coupled into a 550μm diameter (MMF1) f/2.2 (f = 11 mm, numerical aperture 0.22) silica fiber by an f/1.0 lens. The criteria for selecting this fiber are given below in **Beamsteering**. We estimate the power coupled into the 550μm fiber over the 1600 nm to1850 nm range to be 1.8mW (Equation 4 [15]). Note that this implies ~ 0.01% efficiency from input electrical power to optical power useful for the experiment.

Equation 4
$$P_{fiber} = \varepsilon_{lamp} A_{fiber} \int_{1600nm}^{1850nm} \int_{0}^{2\pi} \int_{0}^{\theta_{fiberNA}} I_{\lambda,b} \cos(\theta) \sin(\theta) d\theta d\phi d\lambda$$

Where P_{fiber} [mW] is the power in the fiber, ε_{lamp} [unitless] is the effective emissivity of the lamp, A_{fiber} [m^2] is the core area of the fiber, $\theta_{fiberNA}$ [rad] is the fiber half angle defined by its numerical aperture, $I_{\lambda,b}$ [$Wm^{-2}nm^{-1}sr^{-1}$] is the spectral distribution of a

blackbody at 3200K, θ [rad] is the zenith angle of the emitted light, φ [rad] is the azimuthal angle of the emitted light, and λ [nm] is wavelength.

Light from the 550 μm diameter fiber was collimated by a lens (L2, f/1.9, Thorlabs F220SMA-C) to a 5 mm beam diameter. The engine pitch side optical access port had a 3.8 mm diameter while the catch side had a 1.3 mm diameter. On the catch side, light was focus by a lens (L3, f/0.76, f = 4.5 mm, Thorlabs F230FC-1550) onto a 62.5 μm diameter (MMF2) f/1.7 silica fiber. The transmission of the light from MMF1 to L3 was ~7%.

II.3.1.4 Beamsteering

In spite of the poor coupling efficiency of this approach, it was found that this system was relatively immune to steering due to density gradients in the engine. A discussion of this immunity will begin by discussing the catch fiber (MMF2). MMF2 serves as both the light conduit from the engine and the input slit for the spectrometer. On one hand, the larger the diameter of MMF2, the larger the amount of light collected from the engine. On the other hand, an increase in MMF2 diameter results in a decrease in spectrometer resolution. MMF2 was selected to be a 62.5 μm diameter fiber as a compromise between collection and resolution. MMF1 should be at least the diameter of MMF2 to maximize camera signal. In the case where the diameter of MMF1 and MMF2 are equal, in the absence of beamsteering or Fresnel losses, 100% coupling can be attained, and the resulting camera signal is as high as possible without increasing the temperature or

emissivity of the lamp. However, the harsh environment in the engine diffuses the beam, increasing the divergence across the cylinder. The divergence of the input beam in the absence of beamsteering is termed $\theta_{divergence}$ and the local divergence angle due to beamsteering is termed $\theta_{beamsteering}$ (all divergence values are half-angles). Although $\theta_{beamsteering}$ is dependent upon engine conditions (i.e., compression ratio), the maximum $\theta_{beamsteering}$ for the current engine, $\theta_{max\_beamsteering}$, was estimated to be 1.6° at the catch lens using results from a similar engine [16].

Since $\theta_{beamsteering}$ represents a fluctuating quantity potentially yielding unstable spectra, the optimal design for beam steering immunity is for $\theta_{divergence} >> \theta_{beamsteering}$. In other words, if the constant value of $\theta_{divergence}$ is large relative to $\theta_{beamsteering}$ the beamsteering induced irradiance fluctuations experienced at MMF2 will be small. To this end, MMF1 was chosen to be the largest fiber accessible in the lab (550 μm diameter, $\theta_{divergence}$= 1.4°). Larger fiber is available commercially and could be used in future experiments; however, when the fiber diameter exceeds the dimensions of our thermal emitter (0.8 x 2.3 mm), the thermal emitter size should be increased commensurately.

II.3.2 Engine

The engine for this experiment was an isooctane fueled Ricardo Hydra modular single cylinder four stroke metal engine with overhead cams. The cylinder head was manufactured by general Motors and has a pent roof geometry and contains pressure transducer ports which were cast into opposing sides of the cylinder periphery. Sapphire

rods were adapted to these ports for optical access. Cylinder pressure was measure by a piezoelectric pressure transducer (Kistler 6125B) through the spark plug hole. The remaining engine geometry can be seen in Table II.3.2.

Table II.3.2 Metal engine geometry. CAD aTDC and crank angle degrees and after top dead center respectively.

Compression Ratio	10.95:1
Bore	86 mm (3.39 in)
Stroke	94.6 mm (3.72 in)
Intake Valve Open	360 CAD aTDC
Intake Valve Close	540 CAD aTDC
Exhaust Valve Open	131 CAD aTDC
Exhaust Valve Close	375 CAD aTDC

Since ignition for HCCI combustion is governed by chemical kinetics, the intake conditions for the engine are critical. A list of these conditions is shown in Table II.3.3.

Table II.3.3 Metal engine operating conditions. EGR is exhaust gas recirculation.

Intake Pressure	~97 kPa
Exhaust Pressure	~100 kPa
Coolant Temperature	96°C
Oil Temperature	90°C
Engine Speed	1000 RPM
Engine Fuel	Isooctane
Intake Charge Temperature	327°C
Delivered Air-fuel Ratio	20:1
Fuel Mass Flow Rate	10 mg cycle^{-1}
Diluent Type	EGR
Mean Diluent % (by volume)	40%

The intake air was heated with resistive heaters blanketing intake pipes and tanks, and hot exhaust gas recirculation (EGR) was added to the intake air through static mixing tees. Fuel was injected in to the air/EGR mixture far upstream of the engine giving the fuel time to atomize and mix. A more complete description of the engine test cell and its operation are provided by Chialva[17].

II.3.3 Spectrometer and Camera

Light was collected from the engine by a 62.5 μm fiber and brought to a grating spectrometer (Acton SP-2300i, f/3.9) where the 62.5 μm fiber served as the spectrometer

input slit. This spectrometer is a 0.3 meter Czerny-Turner arrangement which utilized a 300 line mm^{-1} ruled diffraction grating blazed at 500 nm(~12% efficient at 1800nm). A grating with the same line density blazed at 2 μm would have increased the efficiency of the system (~90% efficient at 1800 nm). However, this grating was not available at the time of the experiment. The diffracted light was incident upon the linear pixel array of an extended Indium Gallium Arsenide (x-InGaAs) camera (Princeton Instruments OMA V:1024-2.2). The liquid nitrogen cooled camera array consisted of 1024 pixels, each 25 μm wide and 250 μm tall, with spectral responsivity from ~1.0 to ~2.2 μm. The 16 bit pixel values were recorded approximately every 1.1 ms (every 8 CAD for the engine at 1000 RPM) which corresponded to a spectral rate of 900 spectra $second^{-1}$. The spectral resolution of the sensor system was 0.75 nm (3 cm^{-1}) at 1600nm. Therefore, for the 1600nm to 1850nm range, there were 333 spectral resolution elements. Based on comparing the measured camera signal to the 1.8 mW expected in the 550 μm fiber, we estimate that the optical throughput from MMF1 to the camera was ~ 0.002%. These losses are a combination of effects associated with engine coupling, window fouling, and grating efficiency.

Camera triggering and data collection were accomplished as follows. The engine position was provided by a shaft mounted encoder to a pulse generator (BNC model 555) which then sent a TTL signal to the camera initializing integration. The integration time for this experiment was 166μsec, corresponding to 1 crank angle degree (CAD). A spectrum was recorded by integrating the pixel voltages for the duration of one CAD and this was done every eight CADs throughout each engine cycle.

II.4 Experimental Spectra

In this section spectra are presented for both the preliminary investigation of the near-infrared isooctane absorption spectrum and the fired engine tests.

II.4.1 Isooctane

Since the goal of this experiment was to record H_2O and isooctane absorption spectra in an engine, it was desirable to review previously published spectra for both species. The H_2O vapor $\nu_2 + \nu_3$ combination band ($\lambda_{center} \sim 1875$ nm) has a spectrum which is well documented and can be simulated using HITRAN[18]. However, little information could be found on the spectrum of isooctane vapor. Therefore, the spectrum was measured experimentally, both in a static bench top experiment and in the metal engine under noncombusting intake conditions. The results for the preliminary investigation are shown in Figure II.4.1.

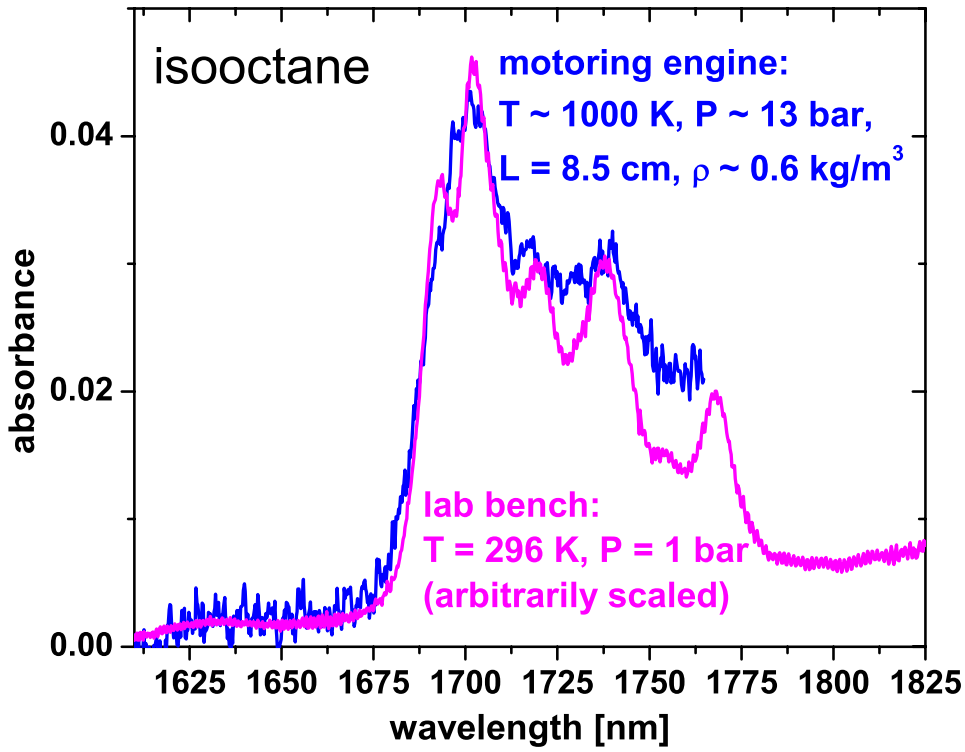

Figure II.4.1 Isooctane absorption spectra, taken with the sensor system, for both vapor under ambient laboratory conditions and in the metal engine under noncombusting intake conditions. The motor engine absorption spectrum was primarily water beyond 1765 nm and was therefore omitted.

In Figure II.4.1 the "lab bench" data was taken with the sensor system through an 11cm high, 6.8cm diameter borosilicate glass vessel. A reference measurement was made through the vessel containing air only at 20°C and 1bar. Next, it was filled with 150mL of liquid isooctane. The vessel was closed and immediately a 10 minute measurement point was taken through the gaseous volume. The data shown in Figure III.4.1 is for an isooctane vapor pressure less than equilibrium. An attempt was made to measure an equilibrium composition absorption spectrum by taking a measurement 12 hours after

closure. However, the lamp spectrum had changed so that the original reference measurement was no longer valid.

The "motoring engine" data in Figure II.4.1 was taken in the engine at -21 CAD after top-dead-center (aTDC) with the intake charge temperature set to 100°C. This temperature is high enough to vaporize the fuel, but not high enough for combustion. This motoring case provided an opportunity to record high pressure and temperature spectra very similar to what would be expected in the fired engine case. Differences in absorption spectra for the different conditions are seen in Figure II.4.1. Most notably, it is seen that an increase in temperature results in a broadening of finer absorption features, consistent with thermal population of higher rotational energy levels in the fuel molecules.

II.4.2 Data collection and emission correction

Once the expected spectra for H_2O and isooctane were known, data were taken in the engine. The engine was brought to steady operating conditions and the sensor system collected spectra. Camera pixel count values were integrated over one CAD, every eight CAD throughout both the compression and gas exchange strokes. This was done for 1000 complete cycles (720 CAD/8 CAD * 1000 cycles = 90,000 spectra). Each respective CAD position spectra was averaged, resulting in 90 spectra.

Next, the lamp was turned off and the data collection procedure was repeated to collect thermal emission spectra. Sample thermal emission spectra are shown in Figure II.4.2.

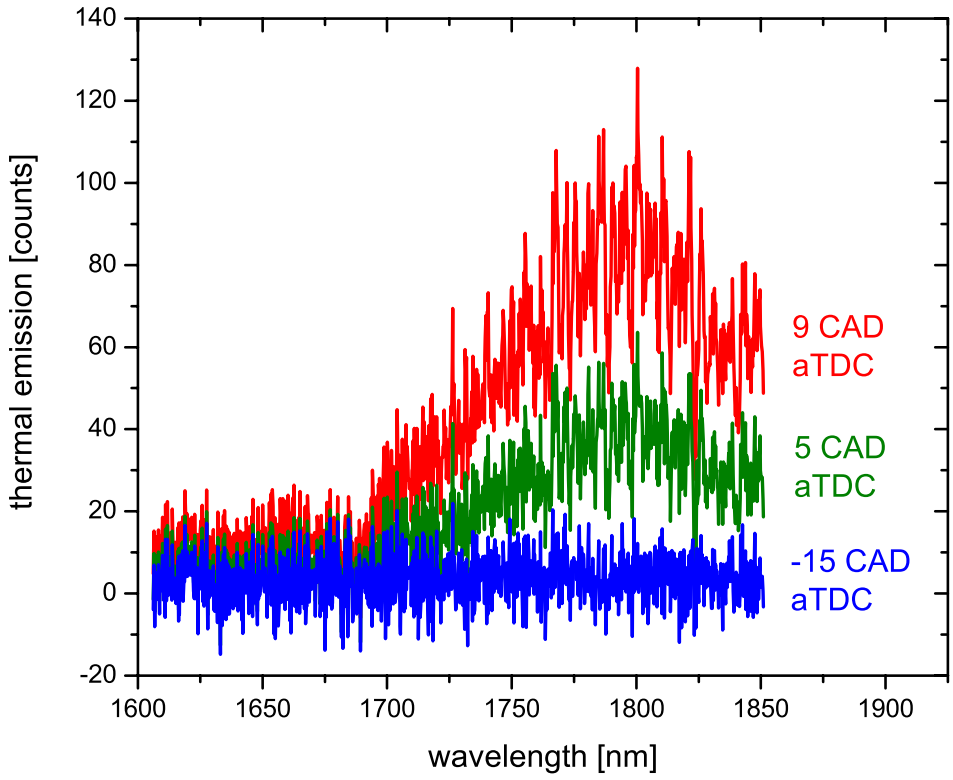

Figure II.4.2 Thermal emission spectra from fired metal engine tests (1000 cycle average). The 9 CAD aTDC data represents the maximum thermal emission, 128 counts at 1800.5nm, which was 37.4% of the collected lamp power at this wavelength.

The 1000 cycle averaged emission spectra were subtracted from the lamp transmission spectra at their respective CAD and wavelengths. The result of this operation was emission corrected transmission spectra, which were next processed using the Beer-Lambert relationship shown in Equation 5.

Equation 5 $$A(\lambda) = -\ln\left[\frac{I(\lambda)}{Io(\lambda)}\right]$$

For the Equation 5, $I(\lambda)$ was the averaged and emission corrected transmitted light for each CAD. $Io(\lambda)$ was the averaged spectra collected immediately after intake valve closure where species densities were the lowest, and therefore providing reference spectra where absorption was a minimum. The minimum detectable absorbance for the 1000 cycle average measurements was less than 1.0%.

The entire preceding procedure was repeated four times at CAD offsets of two degrees. The data sets were then interleaved to produce a single set of absorption spectra for the metal engine at a resolution of two CAD. Both precombustion (a) and combustion (b) spectra are shown in Figure II.4.3.

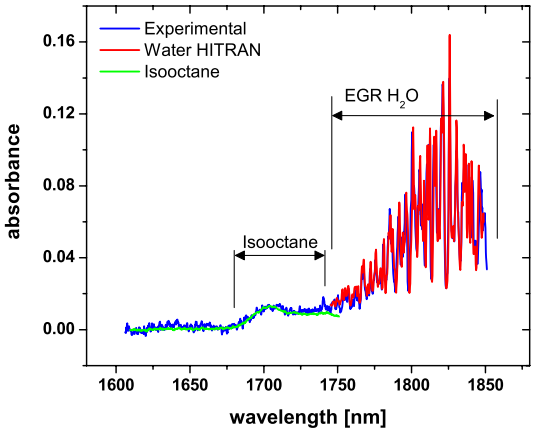

Figure II.4.3 a. Precombustion (-7 CAD aTDC) spectra for metal engine showing isooctane and EGR H2O absorption features. The experimental spectrum is overlaid with both a model fit function of isooctane and the best fit HITRAN spectra for H2O.

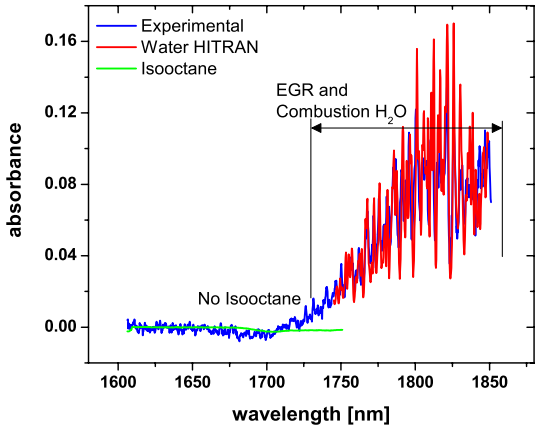

b. Combustion (7 CAD aTDC) spectra showing the destruction of isooctane and the EGR + combustion H_2O absorption feature. The experimental spectrum is overlaid with both a model fit function of isooctane, negligible in this case, and the best fit HITRAN spectra for H_2O.

In Figure II.4.3a, the precombustion absorption spectrum for -7 CAD aTDC is seen which has features for both isooctane and EGR H_2O. Additionally there is a significant nonabsorbing wavelength section, 1600nm to 1675nm, which indicates a reliable measurement baseline. That is, the flat nonabsorbing section illustrates the absence of beamsteering with a chromatic dependence. In the combustion example, Figure II.4.3b, the oxidation of isooctane is shown by the lack of isooctane absorption and the increase in water absorption.

Also seen in Figure II.4.3a and Figure II.4.3b are model fits of the "motoring engine" isooctane spectrum from Figure II.4.1 which was scaled to match the experimental spectra. The resulting scaling factors were later used to determine fuel density as a function of engine position. Likewise, simulated "best fit" HITRAN H_2O spectra are also plotted with the experimental spectra in Figure II.4.3.

The procedure for determining the "best fit" HITRAN H_2O spectra is detailed by Kranendonk et al in[19]. However, a brief description of the process will be given here. First, the portion of the experimental spectrum containing H_2O features was differentiated to remove the potential influence of interfering broad absorbers. Crossover from the isooctane spectrum is an example. Second, the differentiated spectra were compared at measured pressures to differentiated spectra from the HITRAN database. A least squared error method was used to determine the best match. The result of this technique is not only best fit spectra, but also inferred H_2O vapor temperatures and concentrations. The results of both the fuel and H_2O fitting are presented in the following section.

II.5 Results

Figure II.5.1 is a summary of thermodynamic properties inferred from the data collected with the sensor system and the in-cylinder pressure transducer. The properties are shown for a crank angle position from -90 CAD to 10 CAD aTDC. After 10 CAD aTDC, the measurement signal-to-noise ratio was reduced by beamsteering to a level where the fitting technique was no longer reliable.

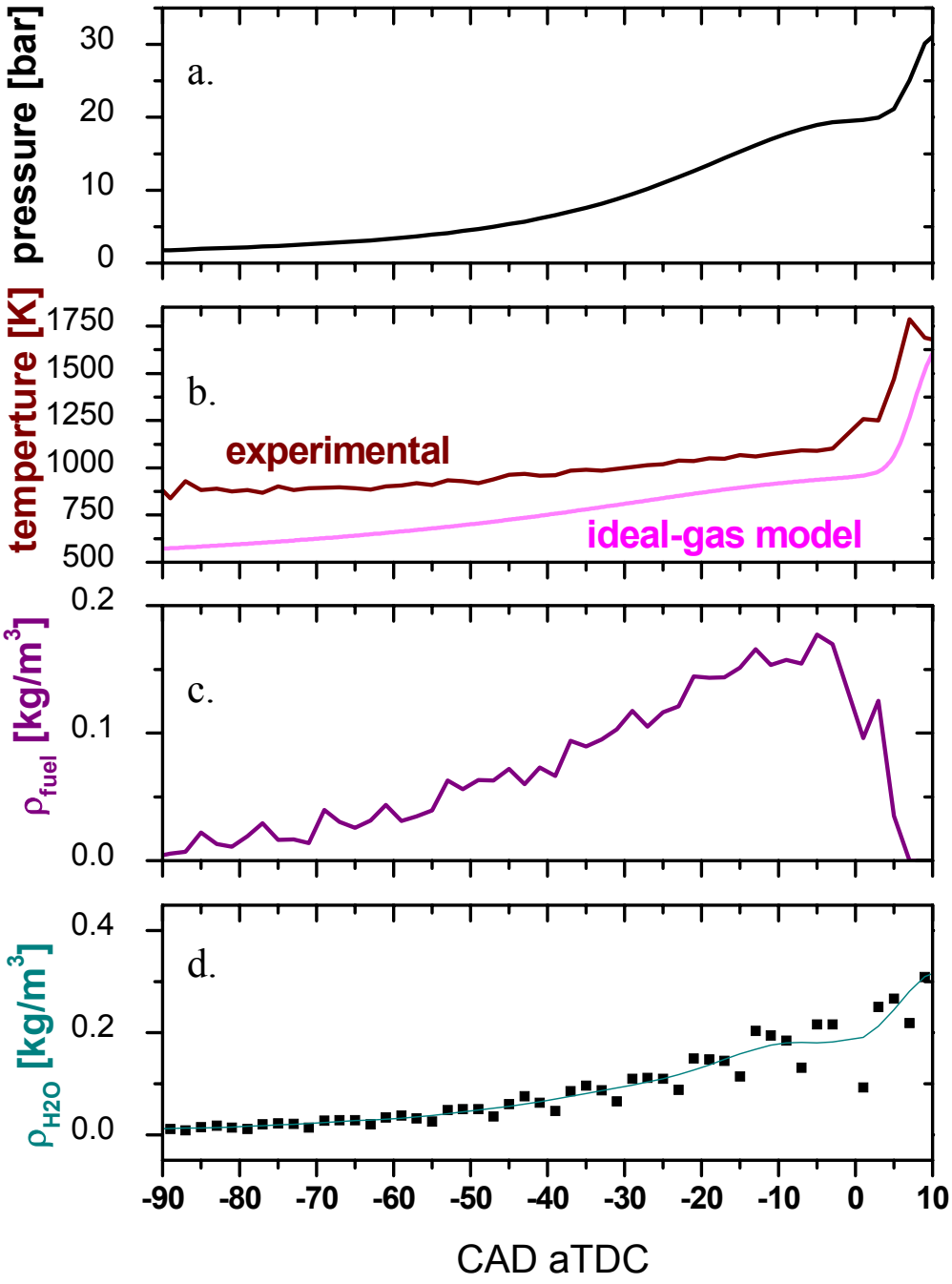

Figure II.5.1 Experimental results (1000 cycle averaged) for the isooctane fueled, 10 mg cycle^{-1}, metal engine running at 1000 RPM with 40% EGR by volume. a) Is the in-cylinder pressure from transducer. b) Is the inferred in-cylinder temperature plotted with an ideal-gas model. c) Is the fuel density from experimental spectra fit. d) Is the inferred H_2O density with a smoothed fit.

Figure II.5.1a shows a typical reciprocating engine compression trace representing early compression until approximately top-dead-center (TDC, 0 CAD aTDC). After TDC a sharp pressure increase is observed indicating the onset of combustion. The same trend is shown in Figure II.5.1b where the inferred experimental in-cylinder temperature is plotted with an ideal gas model. Both temperatures increase at a slight rate due to compression, but more drastically near TDC due to combustion. Although the experimental and model traces in Figure II.5.1b exhibit similar trends, there is an obvious of temperature offset between the two (~160K near TDC). This offset can be eliminated by purging the beam path outside of the engine with dry air or nitrogen. It has been shown that, with refinement, in-cylinder temperature can be determined by this inference technique with an accuracy of ±2%[1].

The density of fuel and H_2O, shown in Figure II.5.1c and Figure II.5.1d respectively, also increase with crank angle during compression as expected. It is seen however, that near TDC the fuel density goes to zero as it was oxidized. Conversely, the H_2O density, which was largely EGR H_2O up to this point, increases due to the formation of combustion H_2O.

Regarding accuracy, the measurement of fuel density was within ±18% of the actual from -45 to -5 CAD aTDC. This uncertainty is attributed to the interleaving of data sets. A camera with increase spectral rate (greater than 6 kHz) would allow spectra to be recorded on a continuous crank angle basis, significantly reducing this error. The water density measurement would also benefit from a faster camera. For example, Kranendonk

et al show that this technique is capable of measuring water concentration to within ±2% when using continuous data.

II.6 Discussion

In this experiment, it was shown that a broad-wavelength source coupled through an HCCI engine and collected by a grating spectrometer is an effective approach for near-infrared spectroscopy. It has also been shown that in-cylinder temperature, fuel density, and H_2O density can be monitored by sensing isooctane (first overtone of C-H stretch) and H_2O ($\nu_2 + \nu_3$ combination band, R branch) absorption spectra. These measurements were made by an optical system with a spectral resolution of 0.75 nm over 1600 nm to 1850 nm at a rate of 900 spectra second^{-1}. It is important to highlight the flexibility of the current approach. The system used in this experiment was capable of measurements anywhere in the 1.0 μm to 2.2 μm range with 100s of nm coverage with resolutions less than 1.0 nm in some cases.

Although lamp and spectrometer measurements are not inherently difficult, measurements in a highly transient and hostile environment such as an engine are challenging. In this paper we have presented multispecies measurements in this environment. However, our approach could be applied for more accurate single cycle measurements with improvements in the following areas. An increase in camera spectral rate would allow data collection at resolutions of 1 CAD or better, eliminating interleaved data sets. A broad-wavelength source with high irradiance, such as supercontinuum [8], would increase the signal-to-noise ratio, permitting single cycle measurements. Also,

since the accuracy of the extrapolated HITRAN simulation database is in question, any improvement in the database accuracy would result in an improvement in the technique presented.

Acknowledgements

The authors thank Mr. Angelo Chialva and Prof. Jaal Ghandhi at the University of Wisconsin-Madison Engine Research Center for the use of their engine and their collaboration on this project. Financial support is acknowledged from the DOE FreedomCAR and Vehicle Technologies University Project# DE-FC26-06NT42628.

References

1. L. A. Kranendonk, R. Huber, J. G. Fujimoto, and S. T. Sanders, "Wavelength-agile H_2O absorption spectrometer for thermometry of general combustion gases," Proc Comb Inst, **31** (2006).

2. Sean Younger, *OH Absorption Spectroscopy to Investigate Light-Load HCCI Combustion,* in Masters, (University of Wisconsin-Madison, 2005).

3. T. R. Meyer, S. Roy, T. N. Anderson, J. D. Miller, V. R. Katta, R. P. Lucht, and J. R. Gord, "Measurements of OH mole fraction and temperature up to 20 kHz by using a diode-laser-based UV absorption sensor," Appl Opt, **44:31**, 6729-40 (2005).

4. R. H. Stanglmaier and C. E. Roberts, "Homogenous charge compression ignition (HCCI): benefits, compromises, and future applications," SAE Paper 1999-01-3682, .

5. C. L. Hagen and S. T. Sanders, "Investigation of Multi-species (H_2O_2 and H_2O) Sensing and Thermometry in an HCCI Engine by Wavelength-Agile Absorption Spectroscopy," Measurement Science and Technology, (2006).

6. L. A. Kranendonk, R. J. Bartula, and S. T. Sanders, "Modeless operation of a wavelength-agile laser by high-speed cavity length changes," Opt Express, **13:5**, 1498-1507 (2005).

7. R. R. Alfano, "The supercontinuum laser source : fundamentals with updated references,", 537 (2006).

8. C. L. Hagen, J. W. Walewski, and S. T. Sanders, "Generation of a continuum extending to the mid-infrared by pumping ZBLAN fiber with an ultrafast 1550-nm source," IEEE Photon Technol Lett, **18:1**, 91 (2006).

9. C. Xia, M. Kumar, O. P. Kulkarni, M. N. Islam, F. L. Terry Jr, M. J. Freeman, M. Poulain, and G. Maze, "Mid-infrared supercontinuum generation to 4.5 μm in ZBLAN fluoride fibers by nanosecond diode pumping," Opt Lett, **31:17**, 2553-5 (2006).

10. C. Lan, A. W. Caswell, L. A. Kranendonk, S. T. Sanders, Y. Urata, and Y. Okura, "19-color H2O absorption spectrometer applied for real-time incylindergas thermometry in an HCCI engine"Anonymous 2007).

11. J. W. Walewski, J. A. Filipa, and S. T. Sanders, "Optical beating in time-resolved spectroscopy. Part I: Theory," Appl Spectrosc, **:In preperation.** (2005).

12. C. L. Hagen and S. T. Sanders, "Application of a Novel White Laser Sensor to an HCCI Engine," SAE, **2006-01-1200** (2006).

13. I. Kaminow, "Polarization in optical fibers," IEEE Journal of Quantum Electronics, **17:1**, 15-22 (1981).

14. J. Hecht, *Understanding Fiber Optics* (Prentice Hall, New Jersey, 2002).

15. F. P. Incropera and D. P. DeWitt, *Introduction to Heat Transfer* (John Wiley & Sons, United States of America, 1990).

16. L. A. Kranendonk and S. T. Sanders, "Optical design in beam steering environments with emphasis on laser transmission measurements," Appl Opt, **44:31**, 6762-6772 (2005).

17. Angelo P. Chialva, *Analysis of Intake Charge Temperature and EGR Stratification Effects on HCCI Combustion ,* in Master of Science, Mechanical Engineering, (University of Wisconsin-Madison, 2006).

18. L. S. Rothman, D. Jacquemart, A. Barbe, D. C. Benner, M. Birk, L. R. Brown, M. R. Carleer, C. Chackerian Jr., K. Chance, L. H. Coudert, V. Dana, V. M. Devi, J. M. Flaud, R. R. Gamache, A. Goldman, J. M. Hartmann, K. W. Jucks, A. G. Maki, J. Y. Mandin, S. T. Massie, J. Orphal, A. Perrin, C. P. Rinsland, M. A. H. Smith, J. Tennyson, R. N. Tolchenov, R. A. Toth, J. Vander Auwera, P. Varanasi, and G.

Wagner, "The HITRAN 2004 molecular spectroscopic database," J Quant Spectrosc Radiat Transfer, **96:2 SPEC ISS**, 139-204 (2005).

19. L. A. Kranendonk, J. W. Walewski, T. Kim, and S. T. Sanders, "Wavelength-agile sensor applied for HCCI engine measurements," Proc Comb Inst, **30**, 1619-1627 (2005).

Appendix III Supercontinuum (SC) Experiment:

Application of a novel white laser sensor to an HCCI engine

Christopher L. Hagen and Scott T. Sanders

III.1 Abstract

A laser-based sensor has been developed which generates short multicolored pulses for use with absorption spectroscopy techniques for the collection of thermodynamic information in an HCCI engine. Our sensor is based on supercontinuum generation which is accomplished by coupling a short-duration, high energy laser pulse (the pump) into fiber optics where colors other than the pump are generated through various nonlinear phenomena. The resulting "white pulse" is then stretched out in time by dispersive media (e.g., another fiber) to a time scale which can be collected by a high speed detector and oscilloscope. Although other multicolored (wavelength agile) laser based techniques generated by scanning mirrors or gratings have been applied to HCCI combustion [1], our supercontinuum approach offers a broad range of wavelengths with both high spectral and high temporal resolution from a source with no moving parts. It is anticipated that our sensor will be capable of probing multiple species per scan in the near future. In this paper, we specifically focus on water absorption measurements in an HCCI engine which are used to infer in-cylinder temperature for the purpose of studying the chemical kinetics which govern the HCCI ignition.

III.2 Introduction

Optical measurement techniques are useful for investigating combustion phenomena because they are nonintrusive and can have very fast response times. In particular, absorption spectroscopy is one such technique where properties such as temperature, pressure, and mole fraction of a gas can be inferred by probing the specimen with a rapid scan of light in wavelength and recording the transmission signal on a temporal basis. This measurement is well suited to HCCI combustion because it is a line-of-sight averaged technique. Another optical line-of-sight averaged measurement was made by Kawahara et al using a fiber-optic based heterodyne interferometer [2]. This approach relies on changes in the index of refraction of combustion gases due to density gradients and requires sensor calibration, whereas the work presented here does not. Currently, neither approach is capable of measuring gas properties locally.

In Kranendonk et al., absorption measurements were made using high speed spectral scans in an HCCI engine by vibrating a low-inertia grating. Although this method is fast, we are proposing a method which is still faster owing to the complete omission of moving parts. Supercontinuum generation, the production of broadband or “white light” pulses produced when an intense picosecond or shorter laser pulse propagates through condensed or gaseous media, was first formally investigated in 1969 [3]. The mechanism by which a monochromatic light pulse forms a multicolor pulse is a topic in nonlinear optics. Specifically, some of the contributing nonlinear effects are: self phase modulation (SPM), four wave mixing, and Raman scattering, all of which are described by Paschotta[4]. The dominant supercontinuum generation effect is dependant on factors

such as laser pump pulse duration, irradiance, and the properties of the medium in which the supercontinuum is generated.

Once created, the polychromatic pulse is stretched in time by a dispersive element, which in our case is a dispersion fiber. The combination of dispersion and supercontinua has previously been used for gas sensing by Sanders[5]. However, to our knowledge, this paper represents the first published account of using dispersed supercontinua for in-cylinder temperature measurements. In the following we detail our approach, show initial results and end with an outlook for this system.

III.3 The Engine

The single-cylinder optical engine investigated here is the same as in our previous work[1][6]. Specifications and operating conditions are provided here for reference. The engine has a Bowditch-style piston that allows lubricant-free operation of the combustion chamber. A spacer ring fitted, between the block and cylinder head, with two diametrically opposed sapphire windows (12 mm diameter, 9-mrad wedge) allows optical access to the combustion chamber. The latter houses a 9.24-cm diameter piston which makes a 7.63 cm stroke resulting in a compression ratio of 9.6:1. The optical path through the cylinder is 9.5 cm long.

The input air to the cylinder was delivered through a critical-orifice assembly set at a flow of 2.1 g/cycle and atmospheric intake pressure. The intake air stream was electrically preheated at 363 K and the temperature of intake and exhaust were monitored with type-K thermocouples. The in-cylinder pressure was monitored with a piezoelectric transducer (Kistler 7063) in combination with a charge amplifier (Kistler 5004).

Transducer, cable and charge amplifier were calibrated as a system with a dead-weight tester. The coolant to the engine was preheated and maintained at 343 K. The n-heptane fuel was injected into the heated intake air 1 m upstream from the intake valve. By so doing a high level of uniformity of the fuel-air mixture was achieved[6]. Intake and exhaust valve open and close timing was 349/-180 and 115/365 CAD aTDC respectively where 0 CAD was defined as TDC for the compression stroke. In the experiments reported here the engine was operated at 600 rpm and an equivalence ratio of $\Phi = 0.25$.

III.4 The Laser

The optical arrangement for the tests is shown schematically in Figure III.4.1.

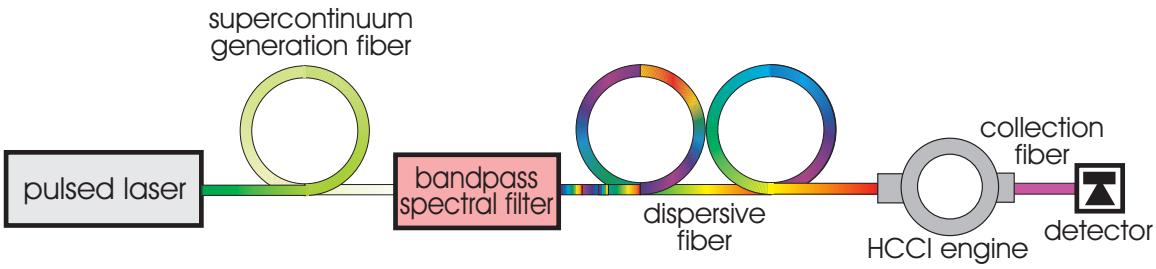

Figure III.4.1 Optical arrangement for HCCI testing.

The laser that we used was centered at 1.56 μm with 1.5 μJ per pulse and an 800 fs duration at a repetition rate of 200 kHz (every 5μs). The supercontinuum generation fiber was a telecommunication grade fiber (Corning Metrocor^{TM}) ~30 cm in length. The core diameter of this standard fiber is 8.1 μm, which is larger than specialty nonlinear fiber (typically ~ 4 μm), and is chosen because it can withstand a significant fraction of the available laser power (~ 1.8 MW) without damaging the fiber ends. The extreme power

over the area of the fiber core, or irradiance, causes short term refractive index changes in the fiber (optical Kerr effect). This process, among other nonlinear processes, contributes to the generation of other wavelengths from the source wavelength. The output spectrum of the supercontinuum generation fiber for our application is shown in Figure III.4.2.

The pump laser wavelength is the obvious peak in both the 5.15 mW and 109 mW examples shown in Figure III.4.2. At the lower power only the original laser wavelengths are present. However, at the higher power new wavelengths are generated as evidenced by spectral broadening.

After the supercontinuum generation fiber, the spectrum is modified by a bandpass spectral filter. In the filter, wavelengths are separated spatially by a diffraction grating.

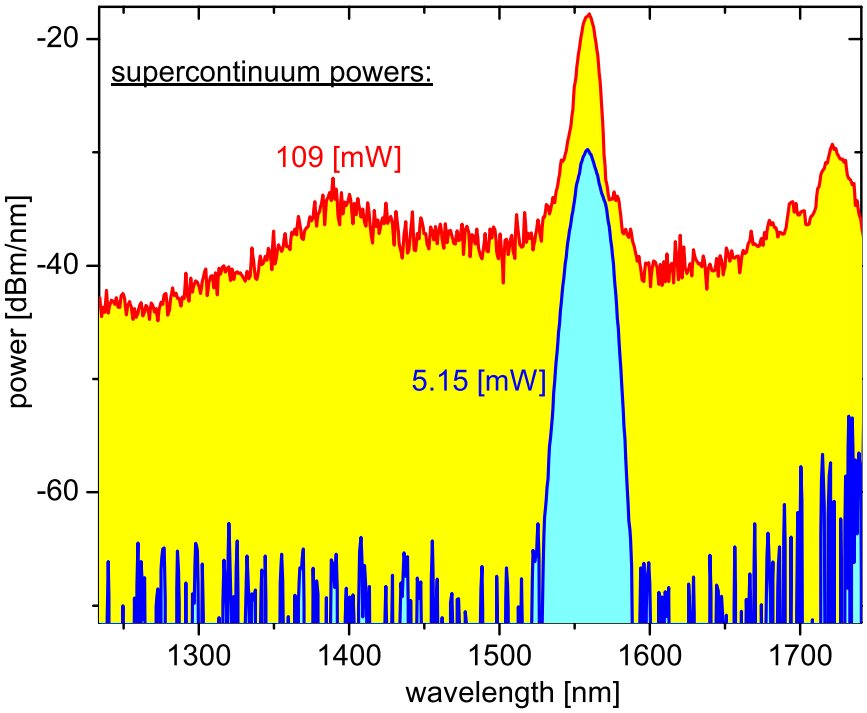

Figure III.4.2 Supercontinuum spectrum.

Once separated, undesirable wavelengths are removed by obstructing their path. For example, the pump wavelength of 1.56 μm is removed to eliminate a residual emission from the laser that occurs in addition to the desired 200 kHz pulse train.

Post-filter light is coupled into a 75-km Metrocor™ dispersion fiber. In this case, dispersion refers to the wavelength-dependant velocity of light propagating through a medium. That is, the wavelengths of the polychromatic light are dispersed in time when traveling through a silica fiber, resulting in a wavelength sweep in time emerging at the

fiber output. Although this effect is negligible in the short supercontinuum-generation fiber, the longer (250,000 times longer) dispersion fiber provides substantial chirping in our experiment. The dispersion of the Metrocor™ at 1450 nm was ~-20 ps/nm-km resulting in a total dispersion in the fiber of ~1500 ps/nm. For example, a pulse with a 100 nm spectral width is stretched to ~ 150 ns.

The dispersed pulse was sent through the engine spacer ring to the collection fiber. A large core (62.5 μm) graded-index multimode fiber was selected to collect the light transmitted through the engine. The purpose of the large area of the collection fiber is to address beam steering issues which can arise when light propagates through a medium with large density and therefore refractive index gradients (e.g., an internal combustion engine)[7]. The light was collected by a 3.5 GHz photoreceiver which was read by a 20 Gs/s (50 ps/pt), 8 bit resolution oscilloscope.

The recorded data is reduced to absorption measurements by use of the Beer-Lambert Law (Eqn. 1):

$$\frac{I}{I_o} = \exp\left(-k_\nu L\right) \qquad \textbf{Eqn. 6}$$

Where I is the transmitted light intensity through the engine, I_o is the initial light intensity, k_ν is the spectral absorption coefficient, and L is the path length. The product $k_\nu L$ is referred to as absorbance. By comparing measured and simulated absorbance spectra, we can infer gas temperature.

III.5 Results

Data were taken during a single fired engine cycle from 33 crank angle degrees before top dead center (CAD bTDC) to 26 CAD after top dead center (aTDC). The laser was pulsed ~2500 times over this range of CADs. The transmitted light was collected and averaged for both precombustion (100 pulses) and combustion (500 pulses) windows. The resulting spectra are shown in Figure III.5.1 below.

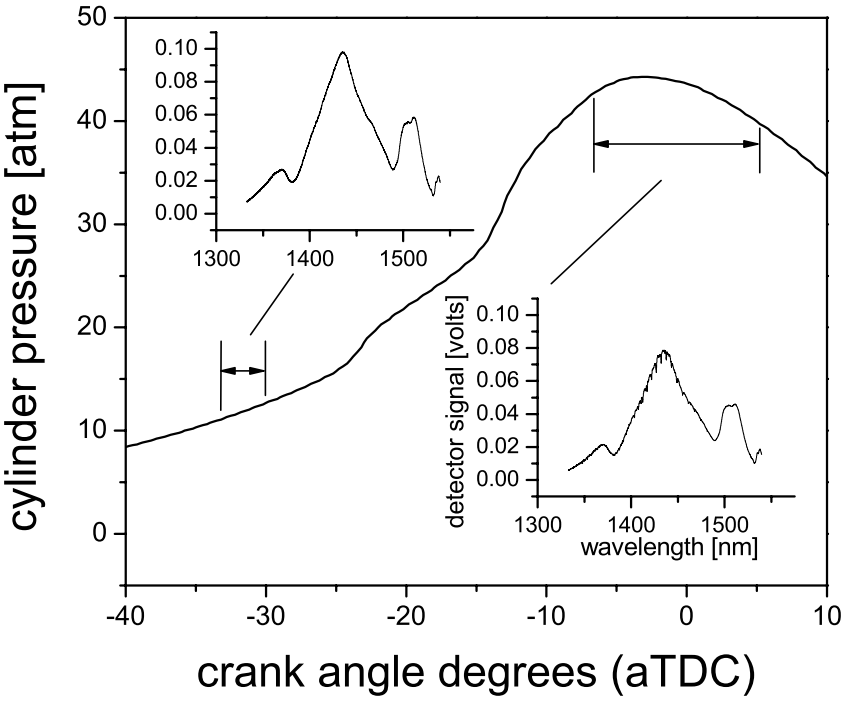

Figure III.5.1 HCCI pressure versus CAD plot with overlays of collected spectra for both precombustion (laser signals averaged -33 to -30 CAD aTDC, Io) and combustion (laser signals averaged -6 to 5 CAD aTDC, I).

The precombustion spectrum in Figure III.5.1 has both a higher signal magnitude and is relatively free of water vapor absorption lines. Because of this lack of water, we chose to use these data as the incident light signal (I_o). In comparison, the combustion trace is slightly attenuated and water absorption is obvious. We believe that the signal attenuation is caused either by beamsteering or another, unidentified, absorber. In any case, the attenuation does not adversely affect our inference of temperature, which

depends only on the sharper features caused by water vapor. The combustion trace is used as the transmitted signal for our analysis (*I*).

The data were processed by applying Beer's law and the results are shown in Figure III.5.2.

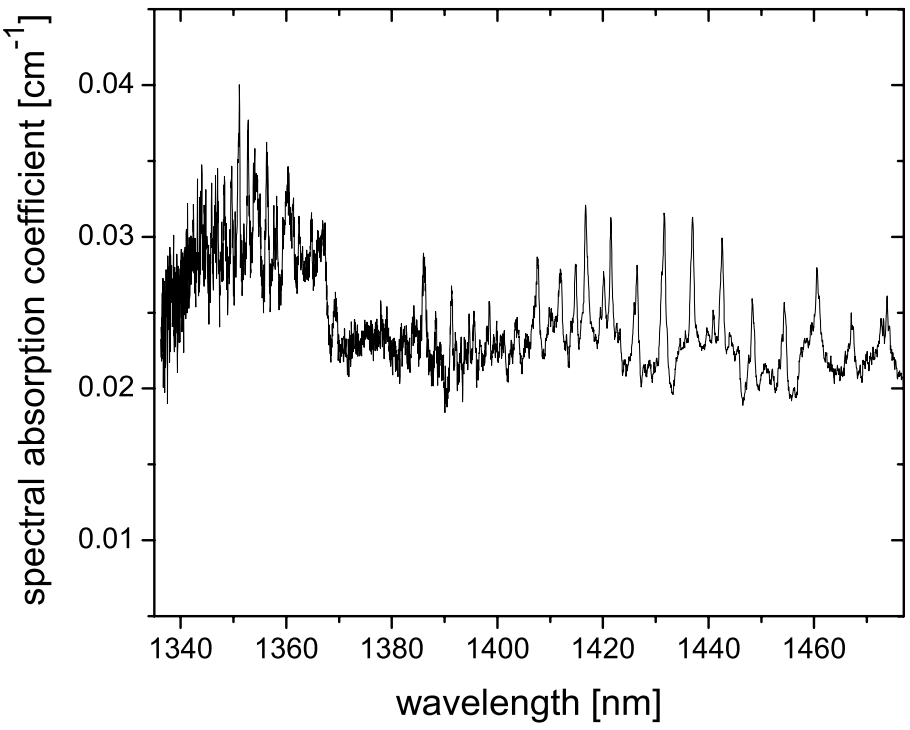

Figure III.5.2 Spectral absorption coefficient spectrum displaying water absorption lines. Also seen are the elevated and uneven baseline which is attributed to beamsteering effects or an unknown broadband absorber.

The data in Figure III.5.2 were differentiated, to remove effects of the imperfect baseline. The resulting spectrum was then compared with the HITEMP [8] water spectra simulation database, as done in Kranendonk [1] to find temperature. Using a least-

squares fit, a computer algorithm determined that the simulated spectrum in our library most closely matching the measured spectrum has a temperature of 1540 K. The experimental spectrum and the theoretical 1540 K spectrum are shown as panels 1 and 3 in Figure III.5.3. For reference, theoretical spectra at 1044 K and 2064 K are also shown to highlight the fact that the 1540 K spectrum does indeed represent a reasonable match to the measured data.

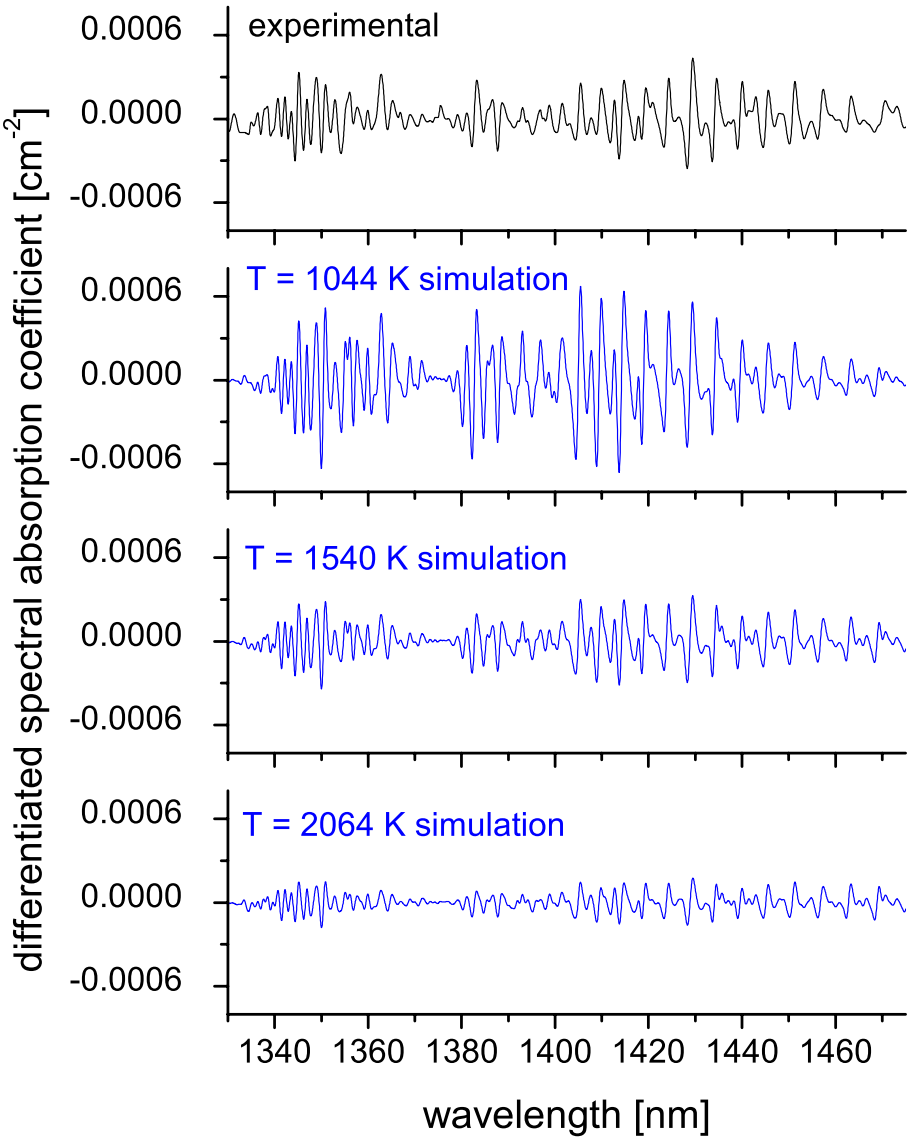

Figure III.5.3 Comparison of experimental and simulated water absorption spectra.

Our data reducing code interpolates between library spectra to obtain a final best-fit temperature of 1510 K near TDC in this engine cycle. Note that this temperature is consistent with previously measured temperatures in the same engine [1]. In our case the

temperature was 1510 K whereas in Kranendonk et al., the temperature was 1350. We believe the two measurements correlate because we expect an increased temperature at an increased equivalence ratio (0.25 for the 1510 K versus 0.16 for the 1350K). Additionally, Kranendonk et al. indicate that the temperature is relatively constant near TDC in this engine, so we feel our averaging is somewhat appropriate.

III.6 Conclusions

We have shown that dispersed supercontinua are a viable chirped light source for determining temperature in an HCCI engine. The absolute accuracy of this method is better than 2%, as in Kranendonk et al, which is dominated by the fitting of the experimental data to the HITEMP database. HITEMP is known to have minor errors; this error contribution would be mitigated by careful absorption measurements in a static heated cell.

A future goal of this project is to improve signal quality to reduce dependence on averaging and, consequently, have the ability to determine temperature reliably from each laser pulse. Another goal is to broaden the source spectrum. We are specifically addressing these challenges by replacing the supercontinuum generation fiber with a similar version containing fused lenses at each end to inhibit optical damage. We are also adding another dispersive element, an achromatic free-space pulse stretcher immediately upstream of the dispersion fiber. The lensed fiber allows increased power coupling which will result in stronger signal and broader spectra. The pulse stretcher will increase the temporal resolution of the collected signal and reduce unwanted nonlinear effects occurring in the dispersion fiber. It is our hope that, with increases in both crank angle

resolution and investigated wavelengths, we will be able to probe HCCI combustion more completely, for example, by monitoring multiple species simultaneously.

acknowledgments

The authors thank Mark Schrewe for his assistance during laboratory testing. This material is based upon work supported by the National Science Foundation under Grant No. CTS-0307455. The authors also gratefully acknowledge financial support of the DOE HCCI Consortium Project contract # DE-FC04-02AL67612.

References

[1] Kranendonk,L.A., Walewski,J.W., Kim,T. and Sanders,S.T., "Wavelength-agile sensor applied for HCCI Engine Measurements"*, Proc. Comb. Symp.* **30**, 1619-1627 (2005).

[2] Kawahara,N., Tomita,E. and Kamakura,H., "Unburned gas temperature measurement in a spark-ignition engine using fibre-optic heterodyne interferometry"*, Meas Sci Technol* **13**, 125-31 (2002).

[3] Alfano,R.R.,"The Supercontinuum Laser Source" **1**, 458 (1989).

[4] Paschotta,R.,"Encyclopedia of Laser Physics and Technology, http://www.rp-photonics.com/encyclopedia.html" **2005** (2005).

[5] Sanders,S.T.,"Wavelength-agile fiber laser using group-velocity dispersion of pulsed super-continua and application to broadband absorption spectroscopy", *Appl.Phys.B* **75**, 799-802 (2002).

[6] Sanders,S.T., Kim,T. and Ghandhi,J.B., "Gas temperature measurements during ignition in an HCCI engine", *SAE 2003-01-0744* (2003).

[7] Kranendonk,L.A. and Sanders,S.T., "Optical design in beam steering environments with emphasis on laser transmission measurements", *Appl. Opt.* **44**, 6762-6772 (2005).

[8] Rothman,L.S., Barbe,A. and Benner,D.C., et al, "The HITRAN molecular spectroscopic database: edition of 2000 including updates through 2001", *J.Quant.Spectrosc.Radiat.Transf.* **82**, 5-44 (2003).

Appendix IV Derivation of $SNR_{photon\ max}$ Using Background Limited Infrared Photodetector Normalized Detectivity or D^*_{BLIP}

$$SNR = \frac{P}{NEP}$$ Signal-to-noise ratio

$$P = A_d \int_{\lambda_1}^{\lambda_2} M_{e,\lambda}(\lambda, T)$$ Power

$$M_{e,\lambda}(\lambda, T) = \frac{2\pi hc^2}{\lambda^5 (e^{\frac{hc}{\lambda kT}} - 1)}$$ Planck's distribution for spectral energy flux density

$$M_{p,\lambda}(\lambda, T) = \frac{2\pi c}{\lambda^4 (e^{\frac{hc}{\lambda kT}} - 1)}$$ Planck's distribution for spectral photon flux density

$$M_{e,\lambda}(\lambda, T) = \frac{hc}{\lambda} M_{p,\lambda}(\lambda, T)$$ Relationship between the flux densities

$$NEP = \frac{\sqrt{A_d \Delta f}}{D^*}$$ Noise equivalent power

$$D^*_{BLIP}(\lambda, f) = \frac{\lambda}{hc} \left(\frac{\eta}{2 \sin \theta_{\frac{1}{2}} \int_0^{\lambda_{max}} M_p(\lambda, T_B) d\lambda} \right)^{\frac{1}{2}}$$

Note:
λ is used here to scale so D* reaches D*(λ_{max}) at λ_{max}

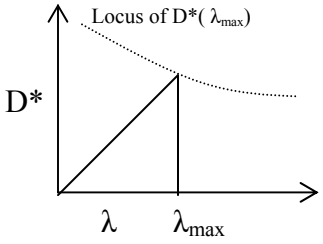

assuming η=1 and $\theta_{1/2}$=90°

$$D^*_{BLIP}(\lambda, f) = \frac{\lambda}{hc} \left(\frac{1}{2 \int_0^{\lambda_{max}} M_p(\lambda, T_B) d\lambda} \right)^{\frac{1}{2}}$$

Substituting NEP, P and D^*_{BLIP} into SNR gives:

$$SNR_{photon} = \frac{PD^*_{BLIP}}{\sqrt{A_d \Delta f}} = \frac{A_d \int_{\lambda_1}^{\lambda_2} M_{e,\lambda}(\lambda,T) \frac{\lambda}{hc} \left(\frac{1}{2\int_0^{\lambda_{\max}} M_p(\lambda,T_B) d\lambda} \right)^{\frac{1}{2}}}{\sqrt{A_d \Delta f}} = \frac{A_d \int_{\lambda_1}^{\lambda_2} \frac{hc}{\lambda} M_{p,\lambda}(\lambda,T) \frac{\lambda}{hc} \left(\frac{1}{2\int_0^{\lambda_{\max}} M_p(\lambda,T_B) d\lambda} \right)^{\frac{1}{2}}}{\sqrt{A_d \Delta f}}$$

If we measure at λ_{max} and integrate over the instrument resolution hc/λ cancels. Also, we consider the following approximation:

$$\int_{\lambda_{\max} - \frac{\Delta\lambda_{res}}{2}}^{\lambda_{\max} + \frac{\Delta\lambda_{res}}{2}} M_{p,\lambda}(\lambda,T_B) d\lambda \approx M_{p,\lambda}(\lambda_{\max},T_B) \Delta\lambda_{res}$$

Therefore,

$$SNR_{photon\max} = \frac{A_d M_{p,\lambda}(\lambda_{\max},T_B) \Delta\lambda_{res} \left(\frac{1}{2M_{p,\lambda}(\lambda_{\max},T_B)\Delta\lambda_{res}} \right)^{\frac{1}{2}}}{\sqrt{A_d \Delta f}} = \sqrt{\frac{M_{p,\lambda}(\lambda_{\max},T_B)\Delta\lambda_{res} A_d}{2\Delta f}}$$

Wien's law:

$$\lambda_{\max} T_{BB} = k_{Wien}$$

Substituting Wien's law into the Planck's distribution for spectral photon flux density:

$$M_{p,\lambda}(\lambda,T) = \frac{2\pi c T_B^{\ 4}}{k_{Wien}^{\ 4} (e^{\frac{hc}{k_{Wien} k}} - 1)}$$

Substituting into the $SNR_{photon\ max}$ equation:

$$SNR_{photon\max} = \sqrt{\frac{2\pi c T_B^{\ 4} \Delta\lambda_{res} A_d}{k_{Wien}^{\ 4} (e^{\frac{hc}{k_{Wien} k}} - 1) 2\Delta f}} = \sqrt{\frac{\pi c T_B^{\ 4} \Delta\lambda_{res} A_d}{k_{Wien}^{\ 4} (e^{\frac{hc}{k_{Wien} k}} - 1) \Delta f}} = \sqrt{\frac{k_1 T_B^{\ 4} \Delta\lambda_{res} A_d}{\Delta f}}$$

Appendix V Guide for Transient Absorption Spectroscopy Measurement System Specifications

Chris Hagen

The following is a rough guide to spectroscopic system specification. The order here is only a suggestion and will likely be unique to the reader's situation. For example, the topic in section 7 may be determined earlier in the process. Also, the list below is used in Christopher L. Hagen's PhD thesis (University of Wisconsin-Madison, 2006) for Chapter 4.

1. Choose Species (or do you just want to measure temperature)

2. Look at the Species Absorption characteristics

That is, find or simulate the approximate absorption spectrum. Useful tools and information are:

- Beer's Law & expected temperature, pressure, mole fraction, and path length
- Spectral databases (HITRAN, etc.)
- Literature search
- Chemkin (chemical kinetics code)

3. Select a Center Wavelength

Now that you have an absorption spectrum, you need to consider the following:

- Absorption strength
- The presence of interfering species
- Practical optics transmission limitations (i.e., transmission of properties of windows, fibers, and lenses. Also, the wavelength responsivity of detector is important.
- Species that absorbs strongly near a center wavelength which is difficult to probe.

Select a preferred center wavelength or absorption band.

4. MDA (determine your minimum detectable absorbance)

Given the information in section 2 and section 3, determine your minimum detectable absorbance.

- That is, decide what an acceptable absorption measurement uncertainty is for your application. This can be based on criteria such as the accuracy of the database from which you will compare the experimental results. If you are attempting to

make direct concentration measurements, determine the acceptable level of uncertainty in concentration and use section 2 to convert this number into MDA.

5. Wavelength Range

Items to consider when the range of wavelengths to measure:

- Measuring multispecies can significantly increase the necessary wavelength measurement range.
- The integrity or "flatness" of the spectrum DC (baseline) is important for direct species concentration measurements. Therefore, it can be necessary to measure nonabsorbing spectral portions to verify baseline integrity. This will increase the required wavelength range.

6. Determine the Time per spectrum

How much time do you have to collect a spectrum?

That is, for a cycle resolved spectral rate for a four stroke engine running at 600 RPM, a spectrum must be recorded once every 278 μs.

Aggregate time: Aggregate time is an important concept for increase signal-to-noise ratio which decreases SNR. For example, engine experiments are, for the sake of the discussion here, repeatable chemical reactions. This means that although a spectrum must be recorded every 278 μs, and identical spectrum can be measured every firing cycle (or 300 time our example engine). The limits here are the time it takes for the windows to foul or the time it takes to data acquisition system to fill it's RAM.

7. Spectral Resolution

Spectral resolution is linked to all of the topics above in some capacity as shown in Christopher L. Hagen's PhD thesis (University of Wisconsin-Madison, 2006). It may or may not be define earlier in the specification process. This is entirely up to the user.

8. Budget?

Once you specify your system, compare its cost to your available funds.